Available online at www.sciencedirect.com

SCIENCE DIRECT®

European Journal of Mechanics B/Fluids 23 (2004) 255–278

Propulsive efficiency of oscillating foils

Laura Guglielmini, Paolo Blondeaux

Environmental Engineering Department, University of Genova, Via Montallegro 1, 16145 Genova, Italy

Received 14 May 2003; received in revised form 16 October 2003; accepted 16 October 2003

Abstract

The dynamics of the vortex structures generated by a foil in steady forward motion, plus a combination of harmonic heaving and pitching oscillations, is determined by means of the numerical solution of the vorticity equation. The force and the torque acting on the foil are also computed. The investigation extends a previous study of the phenomenon (J. Fluid Mech. 410 (2000) 323–341), where only heaving oscillations were considered. The pitching motion turns out to be the only means to produce thrust when the forward motion of the foil vanishes, i.e., for foils operating in the hovering mode. Moreover pitching oscillations added to the heaving motion of the foil produce much larger values of the thrust and better efficiencies. Results are obtained for many combinations of the parameters characterizing the phenomenon and the investigation allows us to identify the range of the parameters providing high propulsive efficiency. The numerical results agree well with previous experimental measurements and, in addition, allow access to the velocity and vorticity fields as functions of space and time, which in turn allows us to identify the underlying thrust production mechanisms more easily.

1. Introduction

Most fishes generate thrust by bending their bodies into a moving wave shape that travels in the direction opposite to the overall forward motion of the fish (Lighthill [1]). This type of swimming is classified according to the amplitude of the overall envelope of the propulsive wave. The anguilliform mode is a purely undulatory mode of swimming in which most or all of the body participates. The side-to-side amplitude of the wave is relatively large along the whole body, even though it may slightly increase toward the tail. In subcarangiform swimmers the side-to-side amplitude of the undulations is small anteriorly and expands significantly in the posterior half of the body. For carangiform swimming the body undulations are further confined to the last part of the body and no complete wavelength is at any time apparent. The carangiform mode is by far the most efficient swimming mode employed in the aquatic environment. Indeed, in this mode, less energy is lost in lateral vortex shedding and thrust is often provided only by a rather stiff caudal fin. Therefore the carangiform mode of propulsion can be studied by focusing our attention on the tail. In the current study we model the tail as a rigid foil and approximate its motion by combining a steady forward motion with heaving and pitching oscillations. Thrust is produced through the formation of a jet which clearly appears downstream of the trailing edge, when the flow is averaged over one period of oscillation. The averaged jet, which is characterized by high momentum, is produced by the periodic shedding of large vortex structures by the tail [2–5]. These vortex structures, which are shed with alternating sign every half cycle, form a staggered array of vortices, which resembles the Karman vortex street observed behind bluff bodies, the only difference being that the vortices rotate in the opposite direction (i.e., reverse Karman vortex street). The flow field and the jet profile depend on the parameters of the problem and, in particular, on the oscillation frequency and amplitude of the tail. Flapping foils have also been investigated as an alternative propulsion device for marine vessels, offering a different paradigm of locomotion than that conventionally used in man-made vehicles. Further investigations of oscillating foils have been made to study the locomotion of insects and birds (see the comprehensive reviews by Maxworthy [6], Ellington [7] and Spedding [8])

The hydrodynamics has been mainly investigated by experimental means because of the difficulties in quantifying vorticity shedding induced by boundary layer separation at the foil surface and in predicting the highly nonlinear dynamics of the large

0997-7546/$ – see front matter © 2003 Elsevier SAS. All rights reserved.
doi:10.1016/j.euromechflu.2003.10.002

vortex structures generated by the roll-up of the free shear layers. Some attempts exist to predict the flow generated by a foil in steady forward motion and performing harmonic transverse and angular oscillations. These attempts are usually based on the assumption of large (strictly infinite) values of the Reynolds number, such that viscous effects have negligible influence on the overall flow and are significant only during the separation process. Hence, the problem becomes one of an inviscid flow. Moreover, the separation at sharp edges is approximated by a Kutta–Joukowski condition and the free shear layers are replaced by concentrated vortices [9] or by vortex panels [10–13]. A three-dimensional nonlinear inviscid numerical approach, in conjunction with experimental data, has been recently used by Zhu et al. [14] to investigate the three-dimensional features of the flow around fish-like bodies. The crux of these approaches lies in choosing the location of the vortex emission and in relating the properties of the shed vortices to the boundary layer characteristics. Moreover, computational costs, which rapidly grow as the number of vortices increases, do not allow long simulations of the phenomenon. Finally, potential flow models simulate vortex shedding by sharp edges but cannot describe possible boundary layer separation from the smooth surface of the foil and the subsequent generation of a free shear layer which can give rise to a vortex structure. In particular, inviscid approaches are unable to describe the leading edge vortices which are experimentally observed when the propulsive efficiency of the foil is maximum.

Investigations of the unsteady flow around airfoils based on the numerical solution of Navier–Stokes (Reynolds averaged Navier–Stokes) and continuity equations have been made within the field of aeronautics and hence the investigated range of the parameters is characterized by high Reynolds numbers and values of the Mach number close to one (Ekaterinaris and Platzer [15]). Moreover small oscillations are usually considered. In studying fish propulsion attention should be focused on moderate values of the Reynolds number and Mach numbers much smaller than one. Furthermore large oscillations should be considered. Recently the flow generated by a foil in steady forward motion with transverse oscillations (no rotation) has been investigated by Wang [16] by means of the numerical integration of the incompressible two-dimensional Navier-Stokes equation. The results obtained by the solution of the full problem demonstrate that optimal flapping frequencies do exist and are associated with leading edge separation. However, as pointed out by Wang [16] herself, a simple heaving oscillation gives rise to low values of the thrust and the modeling of the actual motion of fish tails or insect/bird wings should include both heaving and pitching motions. The major role played by the pitching oscillations in the production of thrust can be understood by considering the wings of an insect in hovering flight. In the absence of any forward motion of the wing heaving oscillations alone cannot generate any thrust because of the symmetry of the problem. In this context pitching oscillations are required to produce thrust (see Section 3.2).

In the current study we determine the flow around a two-dimensional foil whose motion consists of a steady forward component plus harmonic heaving and pitching oscillations. The governing momentum and continuity equations are solved numerically using a stream-function vorticity formulation. The approach considers a two-dimensional problem. Readers familiar with aerodynamic wing theory will recognize that such purely two-dimensional method of calculation overestimates efficiency, because it takes into account only the energy of cross-stream wake vorticity (at right angles to the direction of motion) although in reality trailing vorticity (parallel to the direction of motion) must also be present. However, a two-dimensional approach can provide useful information on the large scale vortical dynamics and on the forces acting on the foil [16].

The problem is formulated in the next section where a brief description of the numerical approach used to determine the solution is also given. The results are described in Section 3 where attention is focused on the propulsive efficiency of the oscillating foil and the dynamics of the shed vortex structures. The final section is devoted to some concluding remarks.

2. Formulation of the problem

A two-dimensional foil in steady forward motion with constant velocity $-\mathbf{U_0}^*$ oscillates with a combination of harmonic heaving and pitching oscillations. Using a reference frame (x^*, y^*) moving with the same forward velocity, the motion of the foil can be described by providing the vertical coordinate $A^*(t^*)$ of the point O around which the foil pitches and the angle $\alpha(t^*)$ (positive in counterclockwise direction) which the foil chord forms with the x^*-axis (see Fig. 1). In the remainder of the paper we will assume that

$$A^*(t^*) = \hat{A}^* \sin(\sigma^* t^*), \tag{1}$$

$$\alpha(t^*) = \bar{\alpha} + \hat{\alpha} \sin(\sigma^* t^* + \varphi), \tag{2}$$

where $\hat{A}^*$ and $\hat{\alpha}$ are the amplitudes of the heaving and pitching oscillations respectively, σ^* is the angular frequency of the oscillations and φ is the phase angle between the two motions. Moreover, $\bar{\alpha}$ denotes the average value of α as taken over one full period of oscillation. If the fluid is characterized by constant density ρ^* and constant kinematic viscosity ν^* then the governing equations of the fluid motion become the vorticity equation and the relationship between the vorticity, denoted ω^*, and the stream function, denoted ψ^*, such that the horizontal and vertical velocity components, denoted u^* and v^* respectively, are

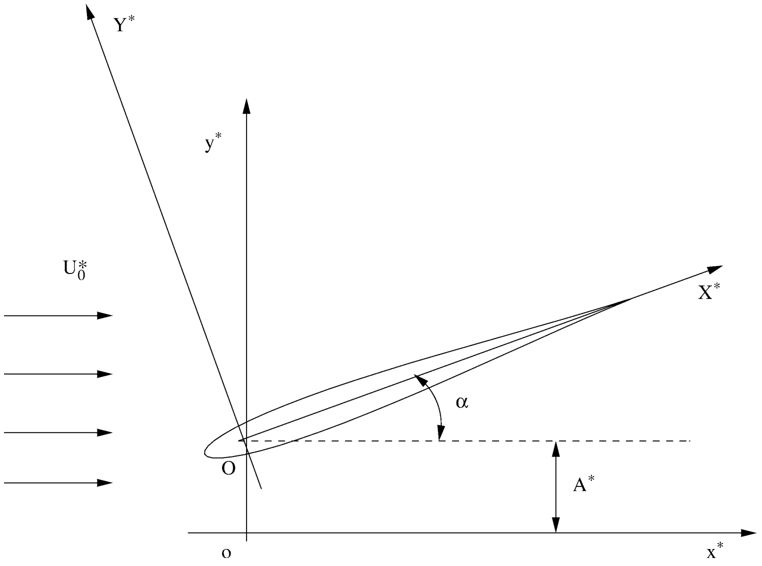

Fig. 1. Reference frame (x^*, y^*) moving with the forward velocity $-\mathbf{U_0}^*$ and reference frame (X^*, Y^*) moving with the foil.

given by $u^* = \partial\psi^*/\partial y^*$, $v^* = -\partial\psi^*/\partial x^*$. The problem is closed by boundary conditions that force the fluid to move with the foil at the foil surface and to be characterized by a velocity $(U_0^*, 0)$ far from the foil. The vorticity and velocity fields are numerically determined following a procedure which makes use of spectral methods and finite difference approximations. To facilitate the numerical computations the problem is posed in a reference frame (X^*, Y^*) that moves with the foil and to this end the new Cartesian coordinates X^* and Y^* are introduced and defined as

$$\big(X^*, Y^*\big) = x^*\big(\cos\alpha(t^*), -\sin\alpha(t^*)\big) + \big[y^* - A^*(t^*)\big]\big(\sin\alpha(t^*), \cos\alpha(t^*)\big). \tag{3}$$

Then, by considering a Joukowski profile, the foil is mapped into a circle of radius $\lambda^* + e^* + s^*$ using the transformation

$$\big(X^*, Y^*\big) = (\xi^*, \eta^*) + \lambda^{*2}\frac{(\xi^* - e^*, -\eta^*)}{(\xi^* - e^*)^2 + \eta^{*2}} + (d^* - e^*, 0), \tag{4}$$

where the lengths λ^*, d^*, e^* are related to the size of the foil, the position of the point O about which the foil pitches and the thickness of the foil respectively. Moreover s^* is a small quantity introduced to round off the trailing edge of the foil. Finally, a polar coordinate system (r^*, θ) is introduced in the plane (ξ^*, η^*) in such a way that the curve $\theta = 0$ gives rise to positive values of ξ^* and vanishing values of η^*.

In the following dimensionless variables

$$\begin{aligned} &t = t^*\sigma^*, \quad r = \frac{r^*}{\lambda^*}, \quad (\xi, \eta) = \frac{(\xi^*, \eta^*)}{\lambda^*}, \quad (X, Y) = \frac{(X^*, Y^*)}{\lambda^*}, \\ &\psi = \frac{\psi^*}{\hat{A}^*\sigma^*\lambda^*}, \quad \omega = \frac{\omega^*\lambda^*}{\hat{A}^*\sigma^*}, \quad A = \frac{A^*}{\lambda^*} \end{aligned} \tag{5}$$

the governing equations become

$$\frac{\partial\omega}{\partial t} + \frac{\hat{A}}{\sqrt{J}}\left[v_r\frac{\partial\omega}{\partial r} + \frac{v_\theta}{r}\frac{\partial\omega}{\partial\theta}\right] = \frac{\hat{A}}{ReJ}\left[\frac{\partial^2\omega}{\partial r^2} + \frac{1}{r}\frac{\partial\omega}{\partial r} + \frac{1}{r^2}\frac{\partial^2\omega}{\partial\theta^2}\right], \tag{6}$$

$$\frac{\partial^2\psi}{\partial r^2} + \frac{1}{r}\frac{\partial\psi}{\partial r} + \frac{1}{r^2}\frac{\partial^2\psi}{\partial\theta^2} = -J\omega, \tag{7}$$

where the radial v_r and azimuthal v_θ velocities are provided by

$$\begin{aligned} (v_r, v_\theta) = \frac{1}{\sqrt{J}}\bigg\{&\left(\frac{1}{r}\frac{\partial\psi}{\partial\theta}, -\frac{\partial\psi}{\partial r}\right) - \frac{1}{\hat{A}}\left[\frac{\mathrm{d}A}{\mathrm{d}t}\sin\alpha - \frac{\mathrm{d}\alpha}{\mathrm{d}t}Y\right]\left[\frac{\partial X}{\partial\xi}(\cos\theta, -\sin\theta) + \frac{\partial X}{\partial\eta}(\sin\theta, \cos\theta)\right] \\ &- \frac{1}{\hat{A}}\left[\frac{\mathrm{d}A}{\mathrm{d}t}\cos\alpha + \frac{\mathrm{d}\alpha}{\mathrm{d}t}X\right]\left[\frac{\partial Y}{\partial\xi}(\cos\theta, -\sin\theta) + \frac{\partial Y}{\partial\eta}(\sin\theta, \cos\theta)\right]\bigg\}, \end{aligned} \tag{8}$$

and J is the Jacobian of the transformation (4)

$$J = 1 + \frac{1 - 2[(\xi - e)^2 - \eta^2]}{[(\xi - e)^2 + \eta^2]^2}. \tag{9}$$

Moreover, the Reynolds number and the dimensionless oscillation amplitude of the foil are defined as

$$Re = \frac{\hat{A}^* \sigma^* \lambda^*}{\nu^*} \quad \text{and} \quad \hat{A} = \frac{\hat{A}^*}{\lambda^*}. \tag{10}$$

The quantity $\hat{A}^*\sigma^*$ has been preferred to U_0^* as velocity scale, because the value U_0^* of the forward speed of the foil can be thought to depend on the propulsive efficiency of the foil itself. The form of the foil depends on the dimensionless parameters $e = e^*/\lambda^*$, which control its thickness, $s = s^*/\lambda^*$, which controls the roundness of the trailing edge and also contributes to the thickness of the foil, and $d = d^*/\lambda^*$, which controls the position of the point O around which the foil pitches.

The boundary conditions force the velocity to vanish on the circle that describes the foil in the (ξ, η) plane and so,

$$v_r = 0, \quad v_\theta = 0 \quad \text{for } r = 1 + e + s. \tag{11a, b}$$

Moreover, far from the cylinder, i.e., for a large value R of r, it should be verified that

$$\begin{aligned}\left(\frac{1}{r}\frac{\partial\psi}{\partial\theta}, \frac{\partial\psi}{\partial r}\right) \longrightarrow{}& U_0 \cos\alpha \left[\frac{\partial Y}{\partial\xi}(-\sin\theta, \cos\theta) + \frac{\partial Y}{\partial\eta}(\cos\theta, \sin\theta)\right] \\ &- U_0 \sin\alpha \left[\frac{\partial X}{\partial\xi}(\sin\theta, -\cos\theta) - \frac{\partial X}{\partial\eta}(\cos\theta, -\sin\theta)\right],\end{aligned} \tag{12a, b}$$

where the dimensionless velocity $U_0 = U_0^*/(\hat{A}^*\sigma^*)$ is the inverse of the reduced frequency, often introduced in the study of oscillating foils.

As previously pointed out, a numerical solution of (6)–(12) is sought. The adopted procedure assumes that (6) and (7) are decoupled: each equation is solved once every time step as the solution is advanced in time. The vorticity transport equation allows us to determine ω at time $t^{n+1} = (n+1)\Delta t$ provided ω is known at the previous time step. Eq. (6) is discretized in space using a grid characterized by constant steps in the z and θ directions, where the variable z is defined by

$$z = \ln(r + b). \tag{13}$$

In this way the r-coordinate is strained using a logarithmic transformation in order to resolve the large velocity gradients occurring near the foil surface. The constant b is a strained parameter which should be properly chosen. For $b = 0$, the transformation given by Eq. (13) defaults to the logarithmic straining used by Braza et al. [17] and Borthwick [18]. The value of b, which appears in Eq. (13), has been fixed in such a way that the dimensional grid size close to the body is always smaller than $0.1\min(\sqrt{2\nu^*/\sigma^*}, \sqrt{4\nu^*\lambda^*/U_0^*})$, where $\sqrt{2\nu^*/\sigma^*}$ and $\sqrt{4\nu^*\lambda^*/U_0^*}$ are the approssimate thickness of the Stokes and Blasius boundary layer respectively. An alternate direction implicit (ADI) method, which decouples the z- and θ-directions, is employed to advance in time. Central differencing is used for diffusive terms while upwind differencing is introduced for the advective terms. The details of the approach, which are omitted here for the sake of space, can be found in text books on numerical approaches (see Hirsh [19] for example). As argued by Leonard [20], numerical viscosity may be important. Therefore, its possible effects have been investigated by successive grid refinements and the results described in the following are not affected by the number of grid points used to discretize (6). To solve the Poisson equation (7), which allows ψ at time t^{n+1} to be determined once ω is known, both ψ and the function $J\omega$ are expanded as Fourier series in the θ-direction.

$$\psi(r, \theta) = \sum_{n=-\mathcal{N}}^{\mathcal{N}} \psi_n(r)\, \mathrm{e}^{\mathrm{i}n\theta}, \tag{14}$$

$$J(r, \theta)\omega(r, \theta) = \sum_{n=-\mathcal{N}}^{\mathcal{N}} F_n(r)\, \mathrm{e}^{\mathrm{i}n\theta}. \tag{15}$$

Substituting Eqs. (14) and (15) into Eq. (7), followed by the use of the relevant orthogonality relations, leads to a set of ordinary differential equations for ψ_n, where F_n are determined by means of a forward FFT algorithm. After having introduced transformation (13), these equations are then discretized using central differences and this leads to a tridiagonal system of linear equations, which must be solved for the ψ_n's. This system can be solved efficiently using the double-sweep algorithm. Then ψ is determined using the inverse FFT algorithm.

In the solution of the Poisson equation for the determination of the stream function boundary conditions given by Eqs. (11a) and (12b) are enforced. The vorticity values at the wall, required during the numerical integration of Eq. (6), are computed using the boundary condition (11b), according to the first-order scheme suggested by Thom [21] and discussed by Roache [22]. Finally a vanishing value of ω is forced at the inflow boundary where the scalar product $\mathbf{v}\cdot\mathbf{n}$ between the fluid velocity $\mathbf{v}$ and the unit vector $\mathbf{n}$, normal to the curve $r=R$ and pointing outward, is negative. On the other hand, at the outflow boundary where $\mathbf{v}\cdot\mathbf{n}$ is positive, the vorticity is forced to have a vanishing normal derivative.

The dimensionless pressure $p=p^*/(\rho^*(\hat{A}^*\sigma^*)^2)$ is not calculated explicitly in the ψ–ω formulation. To obtain the pressure, which is required to determine the force and the torque acting on the foil, momentum equations are used. Along the foil surface, the relative velocity vanishes and the components of the pressure gradient are provided by

$$\left(\frac{\partial p}{\partial X},\frac{\partial p}{\partial Y}\right)=\frac{1}{\hat{A}^2}\left[\frac{\mathrm{d}^2\alpha}{\mathrm{d}t^2}(Y,-X)+\left(\frac{\mathrm{d}\alpha}{\mathrm{d}t}\right)^2(X,Y)+\frac{\mathrm{d}^2A}{\mathrm{d}t^2}(\sin\alpha,-\cos\alpha)\right]+\frac{1}{Re}\left[\frac{\partial^2}{\partial X^2}+\frac{\partial^2}{\partial Y^2}\right](U,V),\tag{16}$$

where U, V are the dimensionless velocity components in the (X,Y) plane. Then the pressure can be obtained by the numerical integration of

$$p(\theta)=p_0+\int_0^\theta\left(\frac{\partial p}{\partial X}\frac{\partial X}{\partial\theta}+\frac{\partial p}{\partial Y}\frac{\partial Y}{\partial\theta}\right)\mathrm{d}\theta,\tag{17}$$

where p_0 is the pressure for $\theta=0$. Finally, it turns out that

$$F_X=\frac{F_X^*}{\rho^*(\hat{A}^*\sigma^*)^2\lambda^*}=\int_0^{2\pi}-p\frac{\partial Y}{\partial\theta}+\frac{2}{Re}\left[\frac{\partial Y}{\partial\theta}\frac{\partial U}{\partial X}-\frac{1}{2}\frac{\partial X}{\partial\theta}\left(\frac{\partial U}{\partial Y}+\frac{\partial V}{\partial X}\right)\right]\mathrm{d}\theta\tag{18}$$

$$F_Y=\frac{F_Y^*}{\rho^*(\hat{A}^*\sigma^*)^2\lambda^*}=\int_0^{2\pi}p\frac{\partial X}{\partial\theta}+\frac{2}{Re}\left[\frac{1}{2}\frac{\partial Y}{\partial\theta}\left(\frac{\partial U}{\partial Y}+\frac{\partial V}{\partial X}\right)-\frac{\partial X}{\partial\theta}\frac{\partial V}{\partial Y}\right]\mathrm{d}\theta\tag{19}$$

$$\begin{aligned}M_Z&=\frac{M_Z^*}{\rho^*(\hat{A}^*\sigma^*)^2\lambda^{*2}}\\&=\int_0^{2\pi}p\left(X\frac{\partial X}{\partial\theta}+Y\frac{\partial Y}{\partial\theta}\right)+\frac{2}{Re}\left[-X\frac{\partial X}{\partial\theta}\frac{\partial V}{\partial Y}+\left(X\frac{\partial Y}{\partial\theta}+Y\frac{\partial X}{\partial\theta}\right)\frac{1}{2}\left(\frac{\partial U}{\partial Y}+\frac{\partial V}{\partial X}\right)-Y\frac{\partial Y}{\partial\theta}\frac{\partial U}{\partial X}\right]\mathrm{d}\theta.\end{aligned}\tag{20}$$

The procedure to obtain F_X, F_Y, M_Z as function of ψ, ω and their derivatives with respect to r, θ is lengthy but straightforward. Details are omitted for the sake of brevity.

3. Discussion of the results

All the results described in the following have been obtained fixing the dimensionless size R of the computational domain equal to 35 and using 300 and 512 grid point in the z and θ directions respectively. Moreover the time step Δt has been fixed on the basis of numerical experiments to ensure the stability of the approach. Some of the runs have been repeated doubling the number of grid points and pratically coincident results have been obtained. All the numerical simulations start with no vorticity and with the fluid and the foil set impulsively in motion with velocity U_0 and according to Eqs. (1) and (2) respectively.

3.1. Validation of the code

In order to check the implementation of the numerical procedure, the investigation of the impulsively started flow around a fixed airfoil has been carried out and the results have been compared with those described in Deng et al. [23], Shen and Loc [24] and Guermond and Quartapelle [25], who solved the problem by means of a mixed finite element approach. In obtaining the results, the velocity scale $\hat{A}^*\sigma^*$ used in relations (5) has been replaced by U_0^* and the time scale $(\sigma^*)^{-1}$ by λ^*/U_0^*. It follows that the problem is posed by Eqs. (6) and (7) with $\hat{A}=1$ and Re replaced by $U_0^*\lambda^*/\nu^*$. The new Reynolds number RE is defined by $RE=U_0^*c^*/\nu^*$, where c^* is the chord lenght. Fig. 2 shows the streamlines for $RE=1000$ and the angle of attack $\bar{\alpha}$ equal to -34°, at $t=6.4$ and $t=14.4$. Moreover, the values of e and s appearing in the transformation (4)

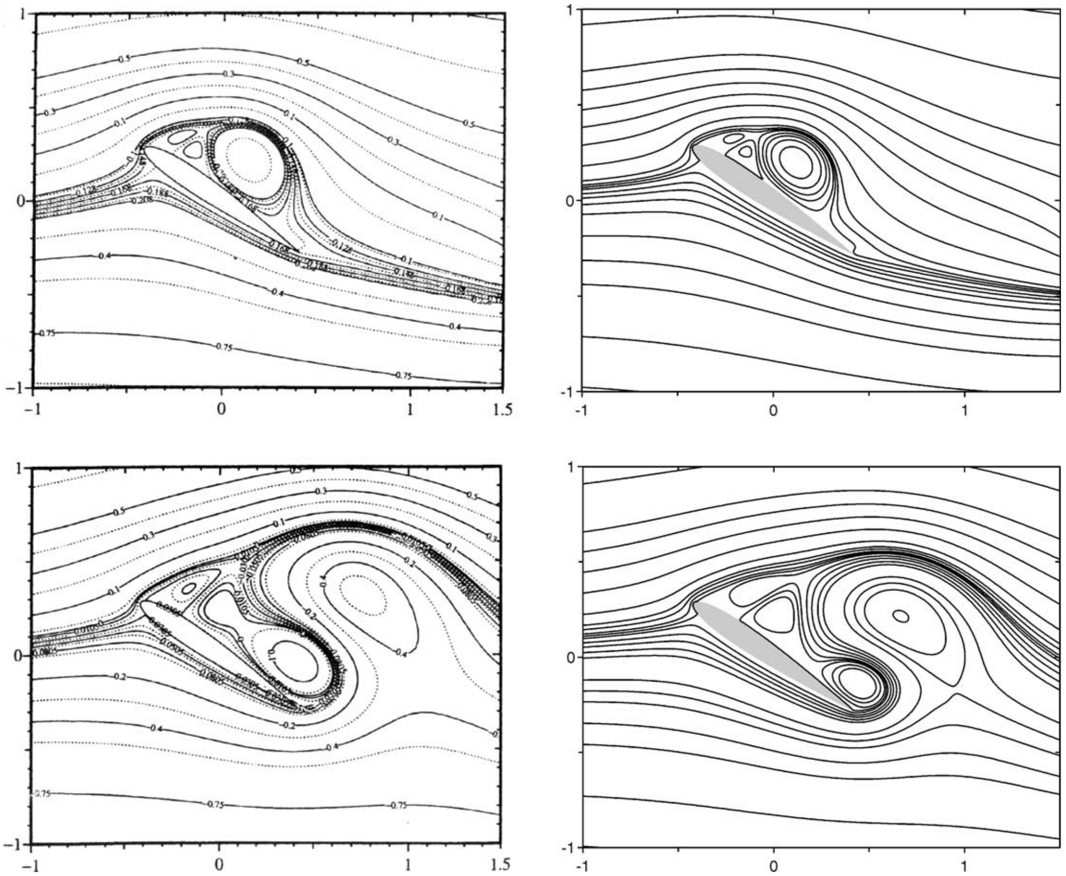

Fig. 2. Impulsively started flow around an airfoil similar to a NACA 0012 airfoil for $\bar{\alpha} = -34^\circ$ and $RE = 1000$. Top row: streamlines at $t = 6.4$; bottom row: streamlines at $t = 14.4$. Left column: Guermond and Quartapelle's [25] results; right column: present results. In the figure the horizontal and vertical coordinates are scaled with the chord lenght.

have been fixed in such a way that the shape of foil differs from that used by Guermond and Quartapelle [25] by an amount always smaller than 1%. Comparing the present results (right side of Fig. 2) with those of Guermond and Quartapelle [25] (left side of Fig. 2), a fair agreement is found, even though some differences in the details of the recirculating regions are present. Also the computed pressure distributions qualitatively and quantitatively agrees with that shown in Fig. 5(a) of Guermond and Quartapelle's paper [25].

A further successful comparison of the present results has been made with those of Wang [16], which used elliptic airfoils. Elliptic airfoils can be presently investigated setting $e = 0$ and choosing an appropriate value of the parameter s. Fig. 3 shows the contour plot of the vorticity at $t = 0.62$, 1.86, 7.48 for $RE = 1000$ and $\bar{\alpha} = -40^\circ$, along with the results of Wang [16] obtained for the same values of the parameters. The agreement is satisfactory. Indeed, the locations of the vortices computed by the present code and shown in the right side of Fig. 3 are practically coincident with those computed by Wang [16] (left side of Fig. 3). For example, the coordinates (X, Y) of the centre of the counter-clockwise vortex at $t = 7.48$ are $(2.95, 1.78)$ when computed by the present code while the coordinates computed by Wang [16] have been estimated to be $(2.9, 1.75)$. Moreover the vorticity values agree well, if the different scaling used by Wang [16] is taken into account.

To further support the obtained results, the flow around an airfoil in steady forward motion and with a combination of harmonic heaving and pitching oscillations has been computed and the results have been compared with the flow visualizations by Anderson et al. [26]. Fig. 4 shows the vorticity field for four different runs at a particular phase of the cycle. It is easy to recognize the vortex structures generated by the roll-up of the free shear layers shed by the leading and trailing edges of the foil and to identify the same vortices visualized by Anderson et al. [26]. The reader should note that to allow an easy comparison between the experimental flow visualization by Anderson et al. [26] and the present numerical results, the mirror image of the latter is shown in Fig. 4. To allow a quantitative comparison, Table 1 shows the maximum value of the time average of the relative strength $|(u - U_0)/U_0|$ of the jet created by the oscillating foil and the thrust coefficient C_T defined in Anderson et al.'s

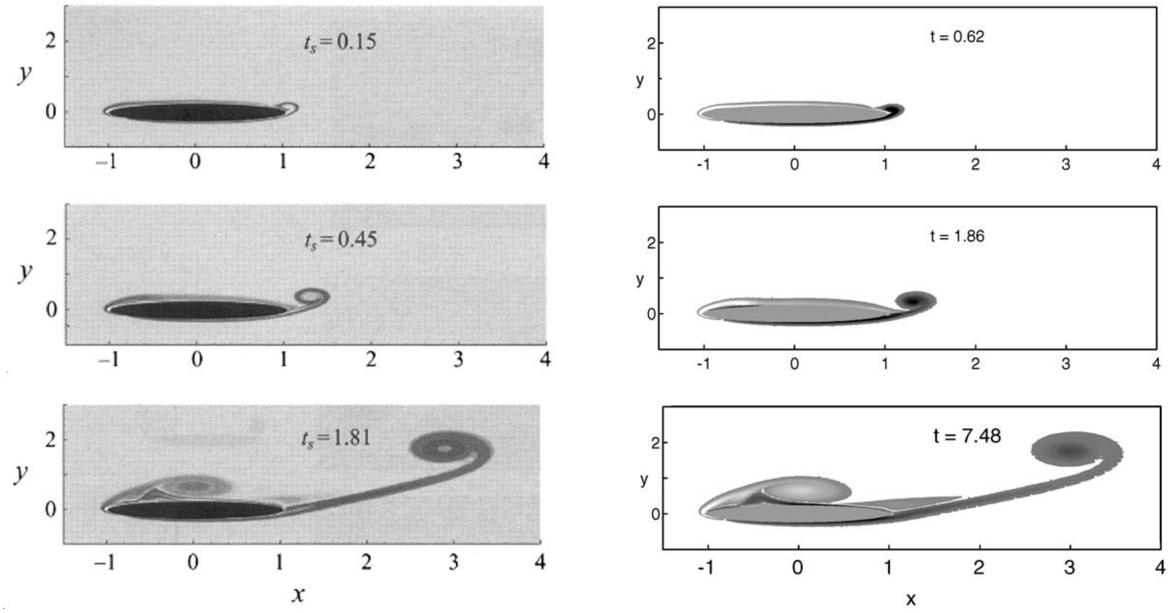

Fig. 3. Vorticity fields around an impulsively started ellipse with angle of attack $\bar{\alpha} = -40°$ and $RE = 1000$, at $t = 0.62$, 1.86, 7.48. Left column: Wang's [16] results; right column: present results. In the figure the horizontal and vertical coordinates are scaled with half the chord lenght and $t_s = t/4.13$.

Table 1
Averaged maximum velocity defect in the wake of the foil and thrust coefficient measured by Anderson et al. [26] and computed by means of the present code

St	$\hat{A}$	$\hat{\alpha}$ (°)	φ (°)	$\lvert\overline{\frac{u-U}{U}}\rvert_{\max}$ (*)	$\lvert\overline{\frac{u-U}{U}}\rvert_{\max}$ (**)	c_T (*)	c_T (**)
0.30	1.0	15	90	0.52	0.40	0.56	0.77
0.32	3.0	30	75	0.16	0.13	0.54	0.34
0.32	3.0	30	90	0.14	0.15	0.48	0.70
0.32	3.0	30	105	0.16	0.17	0.49	0.77

(*) Present results.
(**) Anderson et al.'s results.

paper [26] computed by means of the present code and estimated by Anderson et al. [26] on the basis of their visualizations. The differences in the value of $|(u - U_0)/U_0|$ are less than 20% while those in the value of c_T are larger. The discrepancy between the numerical and experimental values of c_T can be ascribed at the inaccurate procedure used by Anderson et al. [26] to evaluate C_T.

3.2. *Hovering oscillating foils*

Once the reliability and accuracy of the numerical procedure has been ascertained, the investigation of the flow around an oscillating foil has been carried out and the force acting on the foil has been determined.

First, the case of a hovering oscillating foil has been considered. The investigation of the flow generated by a foil which oscillates and pitches without any steady forward motion ($U_0 = 0$) provides information on the flight of hovering insects and allows us to enlighten the major role played by pitching oscillations in providing a positive thrust. To compare present results with those of Wang [16], e has been set equal to zero in such a way that the foil profile turns out to be elliptic. Fig. 5 shows the vorticity fields for $s = 0.291$, $d = 0.667$, $\overline{\alpha} = 0°$, $\hat{A} = 1$, $\hat{\alpha} = -15°$, $\phi = 80°$ and $Re = 260$ at different phases of the cycle and in Fig. 6 the thrust F_x and the y-component F_y of the force are plotted versus time. Similar results are shown in Figs. 7 and 8 but for $\hat{\alpha} = 0°$, i.e., for a foil which oscillates in the transverse direction but does not pitch. In the latter case, as suggested by the symmetry of the problem, the time averaged value of the thrust generated by the foil vanishes. Simultaneously a large force should be exerted on the foil to keep it in motion and the input power is dissipated by the vortices shed by the tips of the foil.

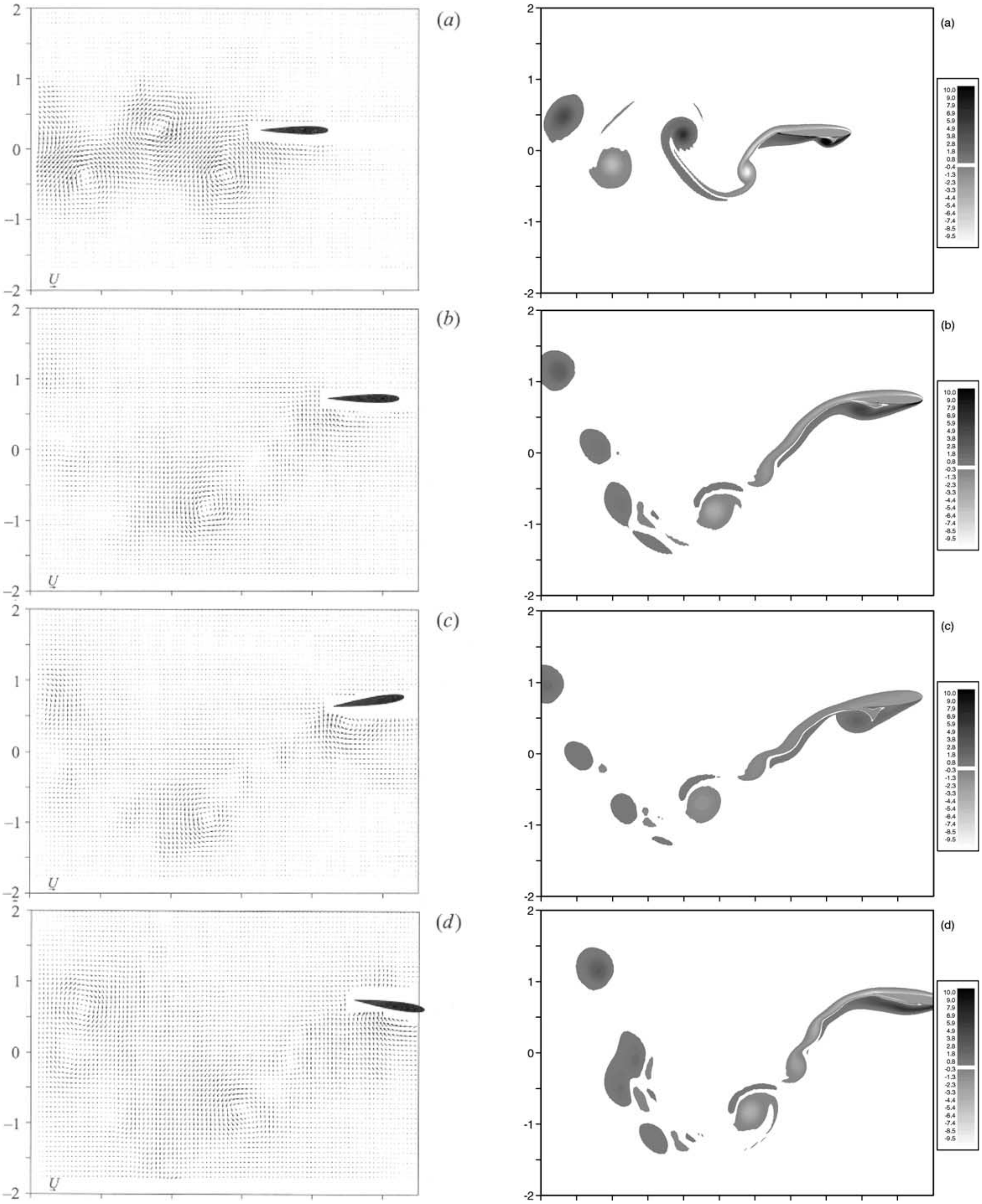

Fig. 4. Vorticity fields when the foil is at its maximum heave position, for $RE = 1100$, (a) $St = 0.3$, $\hat{\alpha} = -15°$, $\hat{A}/4 = 0.25$, $\varphi = 90°$, (b) $St = 0.32$, $\hat{\alpha} = -30°$, $\hat{A}/4 = 0.75$, $\varphi = 90°$, (c) $St = 0.32$, $\hat{\alpha} = -30°$, $\hat{A}/4 = 0.75$, $\varphi = 75°$, (d) $St = 0.32$, $\hat{\alpha} = -30°$, $\hat{A}/4 = 0.75$, $\varphi = 105°$. Left column: DPIV flow visualisation of Anderson et al. [26]; right column: present numerical results. In the figure the horizontal and vertical coordinates are scaled with the chord length.

Similarly a significant input power is required to generate the motion of the foil which pitches and oscillates. However, in this case, thrust is generated. The thrust can be thought to balance the weight of an insect in hovering flight, if the foil is supposed to mimic the motion of its wings. Looking at Figs. 6 and 8 it appears that the periodic motion of the foil generates an aperiod

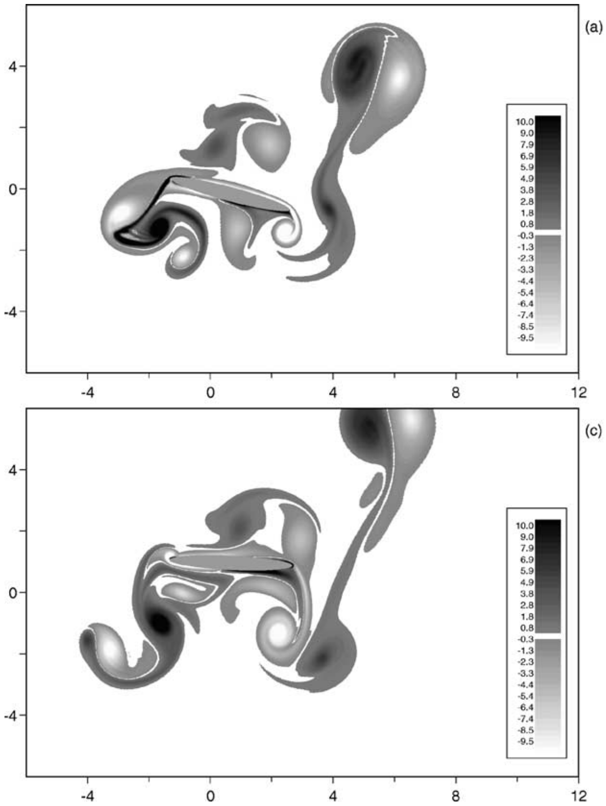

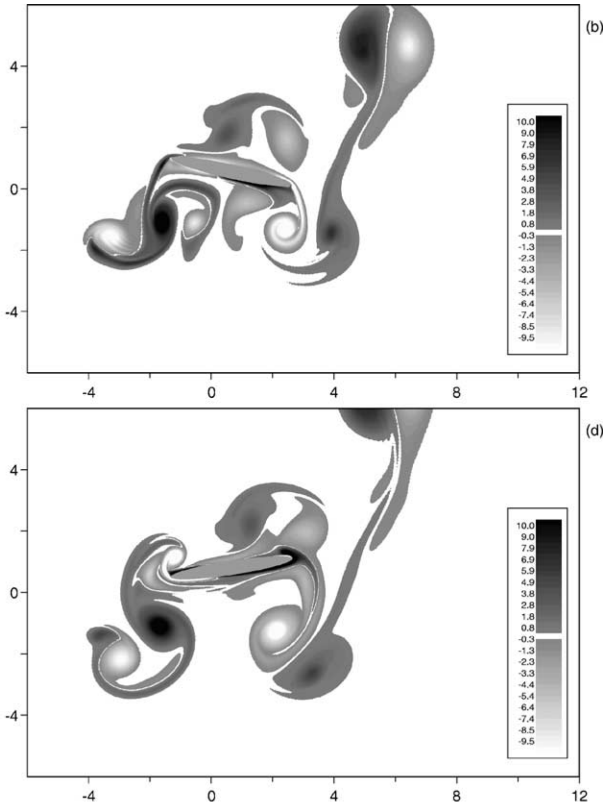

Fig. 5. Vorticity distribution along the foil profile, for $e = 0$, $s = 0.291$, $d = 0.667$, $Re = 260$, $\bar{\alpha} = 0^\circ$, $\hat{A} = 1$, $\varphi = 80^\circ$, $U_0 = 0$, $\hat{\alpha} = -15^\circ$, at (a) $t = 12.566$, (b) $t = 13.352$, (c) $t = 14.137$, (d) $t = 14.923$.

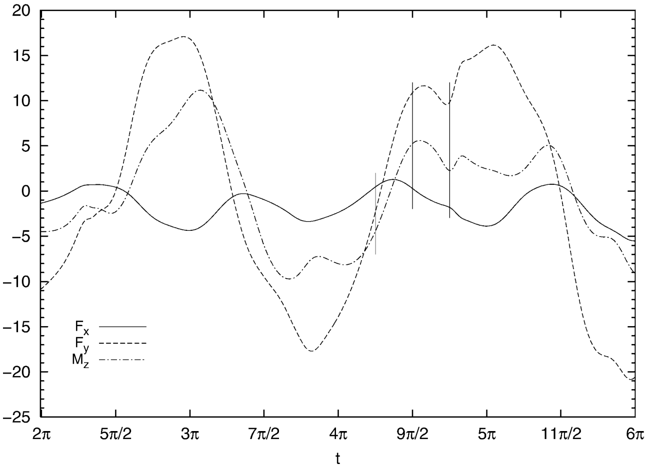

Fig. 6. Forces development on the foil during two periods, for $e = 0$, $s = 0.291$, $d = 0.667$, $Re = 260$, $\bar{\alpha} = 0^\circ$, $\hat{A} = 1$, $\varphi = 80^\circ$, $U_0 = 0$, $\hat{\alpha} = -15^\circ$.

flow. This finding is not surprising because of the highly nonlinear dynamics of the vortex structures shed by the foil which can generate a chaotic flow as shown by the works of Blondeaux and Vittori [27] and Vittori and Blondeaux [28]. The investigation of the optimal motion of the wings of an insect in hovering flight is not performed during the present work which is focused on the propulsive efficiency of the motion of fish tails.

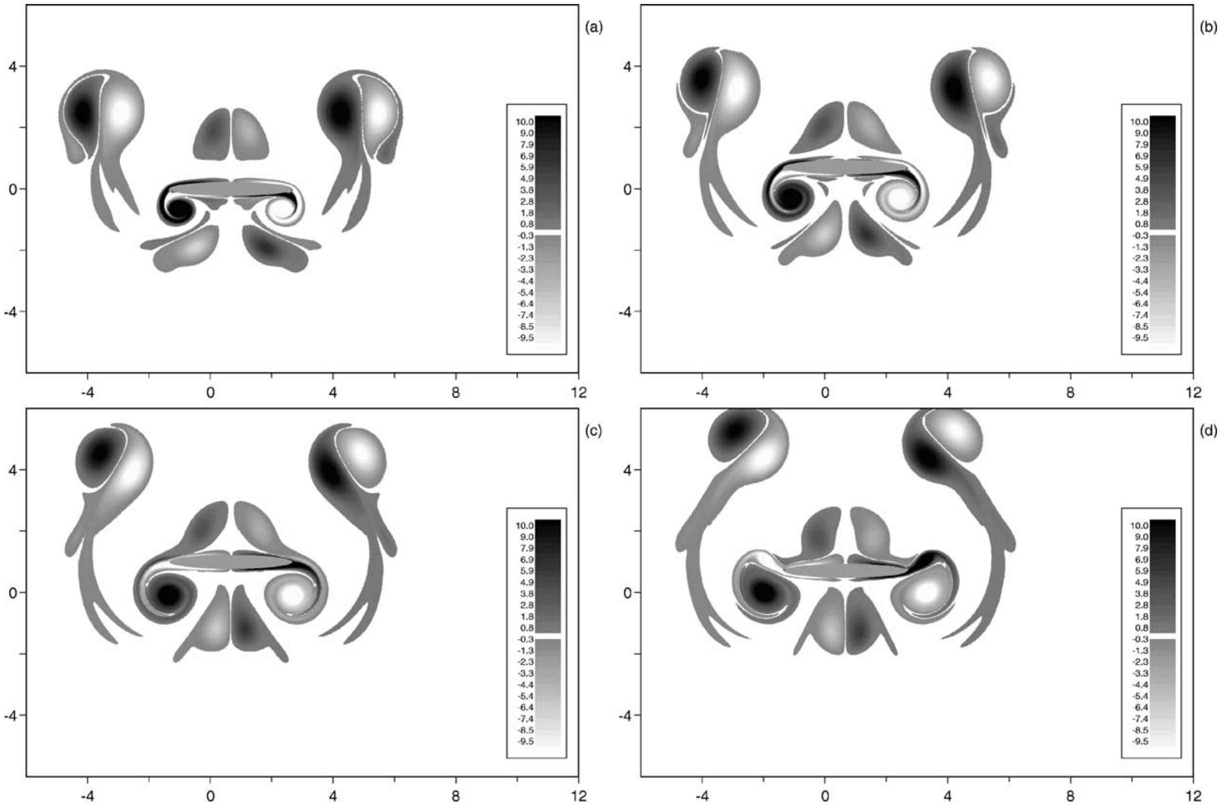

Fig. 7. Vorticity distribution along the foil profile, for $e = 0$, $s = 0.291$, $Re = 260$, $\bar{\alpha} = 0°$, $\hat{A} = 1$, $\varphi = 80°$, $U_0 = 0$, $\hat{\alpha} = 0°$, at (a) $t = 12.566$, (b) $t = 13.352$, (c) $t = 14.137$, (d) $t = 14.923$.

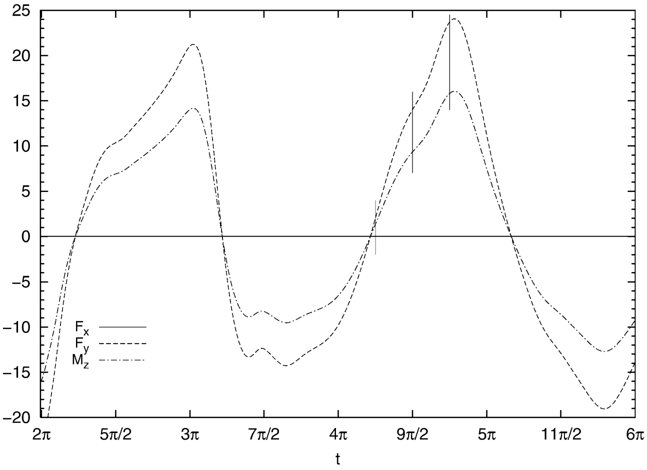

Fig. 8. Forces development on the foil during two periods, for $e = 0$, $s = 0.291$, $Re = 260$, $\bar{\alpha} = 0°$, $\hat{A} = 1$, $\varphi = 80°$, $U_0 = 0$, $\hat{\alpha} = 0°$.

3.3. Propulsive efficiency of oscillating foils

As in Anderson et al. [26], we denote by $\overline{F^*}$ the time average value of F_x^* and with $\overline{P^*}$ the average input power per cycle, i.e.,

$$\overline{F^*} = \frac{1}{T^*} \int_0^{T^*} F_x^*(t^*)\,\mathrm{d}t^*, \tag{21}$$

$$\overline{P^*} = -\frac{1}{T^*} \left(\int_0^{T^*} F_y^*(t^*) \frac{\mathrm{d}h^*}{\mathrm{d}t^*}\,\mathrm{d}t^* + \int_0^{T^*} M_z^*(t^*) \frac{\mathrm{d}\alpha}{\mathrm{d}t^*}\,\mathrm{d}t^* \right), \tag{22}$$

where T^* is the period of oscillation. Moreover, we introduce the power coefficient c_P and the thrust coefficient c_T

$$c_P = \frac{\overline{P^*}}{(1/2)\rho^* 4\lambda^* U_0^{*3}}, \qquad c_T = -\frac{\overline{F^*}}{(1/2)\rho^* 4\lambda^* U_0^{*2}}. \tag{23}$$

Finally the propulsive efficiency η_P is computed as the ratio of the useful power over the input power, as

$$\eta_P = -\frac{\overline{F^*} U_0^*}{\overline{P^*}} \tag{24}$$

so that $\eta_P = c_T/c_P$.

As it appears by the formulation of the problem, there are seven principal parameters which control the results in addition to the shape of the foil, namely: (1) the dimensionless heave amplitude $\hat{A}$, (2) the average angle of attack $\bar{\alpha}$, (3) the pitch amplitude $\hat{\alpha}$, (4) the phase angle φ between the heave and pitch oscillations, (5) the geometrical parameter d, (6) the dimensionless velocity of the foil $U_0 = U_0^*/(\hat{A}^*\sigma^*)$, (7) the Reynolds number. Quite often the dimensionless velocity U_0 of the foil is replaced by the Strouhal number St defined as

$$St = \frac{1}{\pi U_0}. \tag{25}$$

A further parameter of importance for the performances of an oscillating foil is the maximum nominal angle of attack. If $\gamma(t)$ denotes the instantaneous angle of attack, referenced at the pivot point, then, as in [26],

$$\tan\bigl[\gamma(t) + \alpha(t)\bigr] = \frac{1}{U_0} \frac{\mathrm{d}A(t)}{\mathrm{d}t} \tag{26}$$

and the maximum value of $\gamma(t)$, which is presently determined numerically, is denoted as $\gamma_{\max}$.

A first set of numerical simulations as been carried out considering an airfoil characterized by $e = 0.065$, $s = 0.0505$ and keeping fixed the distance of the pivot point from the leading edge ($d = 0.667$). Then, as in Anderson et al. [26], $\hat{A}$ has been

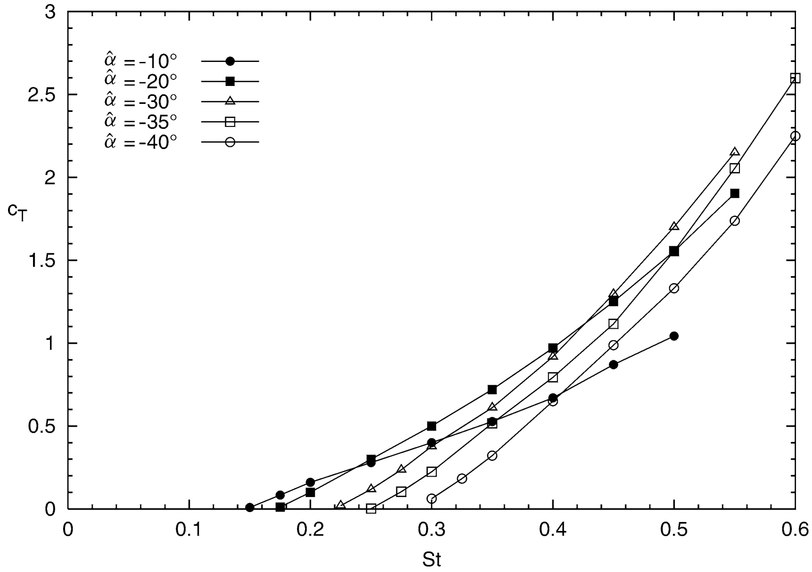

Fig. 9. Thrust coefficient c_T plotted versus the Strouhal number for $RE = 1100$, $\bar{\alpha} = 0°$, $\hat{A} = 3$, $\varphi = 90°$ and different values of the pitching amplitude $\hat{\alpha}$.

fixed equal to 3, $\bar{\alpha}$ equal to zero and $\varphi = 90°$. Different values of the pitch amplitude have been considered ($\hat{\alpha}$ equal to $-10°$, $-20°$, $-30°$, $-35°$ and $-40°$) and $RE = U_0^* 4\lambda^*/\nu^*$ has been kept fixed and equal to 1100. In Fig. 9 the thrust coefficient c_T is plotted versus the Strouhal number, while Fig. 10 shows the propulsive efficiency η_P. The curves of the propulsive efficiency plotted versus the Strouhal number *St* and for fixed values of $\hat{\alpha}$ are characterized by a maximum for a value $St_{\max}$ of *St* falling between 0.25 and 0.4. The peak is present at $St = 0.25$ for the smallest simulated value of $\hat{\alpha}$ ($\hat{\alpha} = -10°$) and then it moves to larger Strouhal numbers when $\hat{\alpha}$ is increased. At small values of $\hat{\alpha}$ the propulsive efficiency is poor, but it increases when $\hat{\alpha}$ is increased till a value of $\hat{\alpha}$ equal to about $-35°$. Then, further increases of $\hat{\alpha}$ lead to a small decrease of η_P. Hence, the highest propulsive efficiency is found for angles ranging around $-30° \div -40°$ and for *St* ranging between 0.3 and 0.4, values

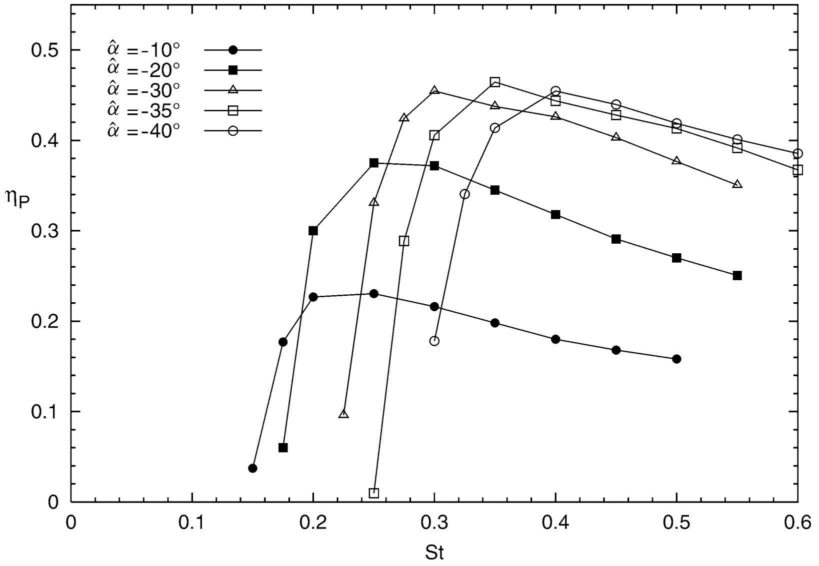

Fig. 10. Efficiency η_P plotted versus the Strouhal number, for $RE = 1100$, $\bar{\alpha} = 0°$, $\hat{A} = 3$, $\varphi = 90°$ and different values of the pitching amplitude $\hat{\alpha}$.

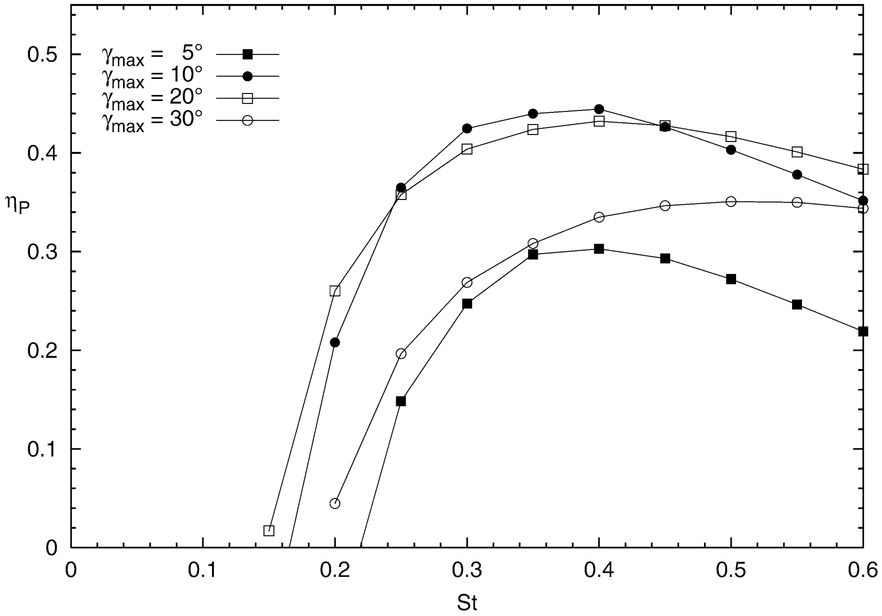

Fig. 11. Efficiency η_P plotted versus the Strouhal numbers, for $RE = 1100$, $\bar{\alpha} = 0°$, $\hat{A} = 3$, $\varphi = 90°$ and different values of the angle of attack $\gamma_{\max}$.

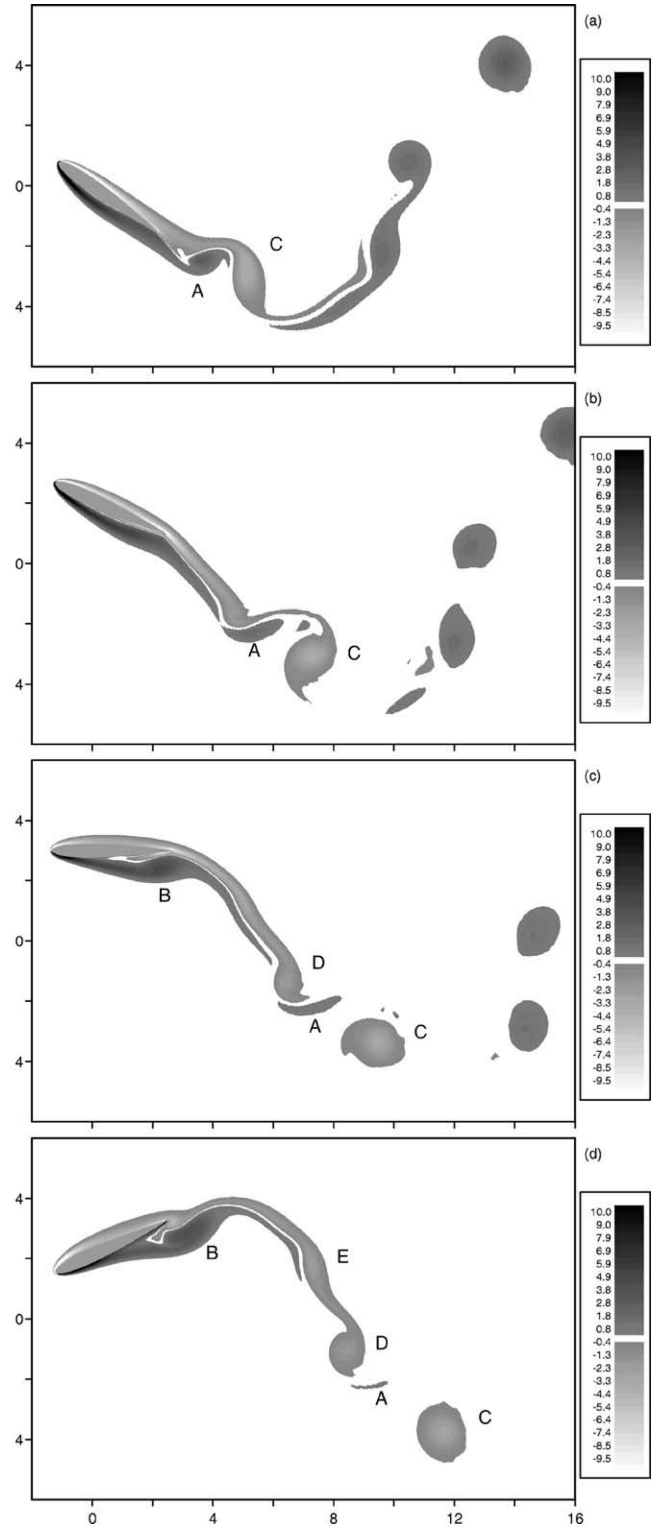

Fig. 12. Vorticity fields for $RE = 1100$, $\bar{\alpha} = 0^\circ$, $\hat{A} = 3$, $\hat{\alpha} = -35^\circ$, $\varphi = 90^\circ$, $St = 0.35$, $\eta_P = 0.46$, $c_T = 0.517$, at (a) $t = 12.566$, (b) $t = 13.352$, (c) $t = 14.137$, (d) $t = 14.923$.

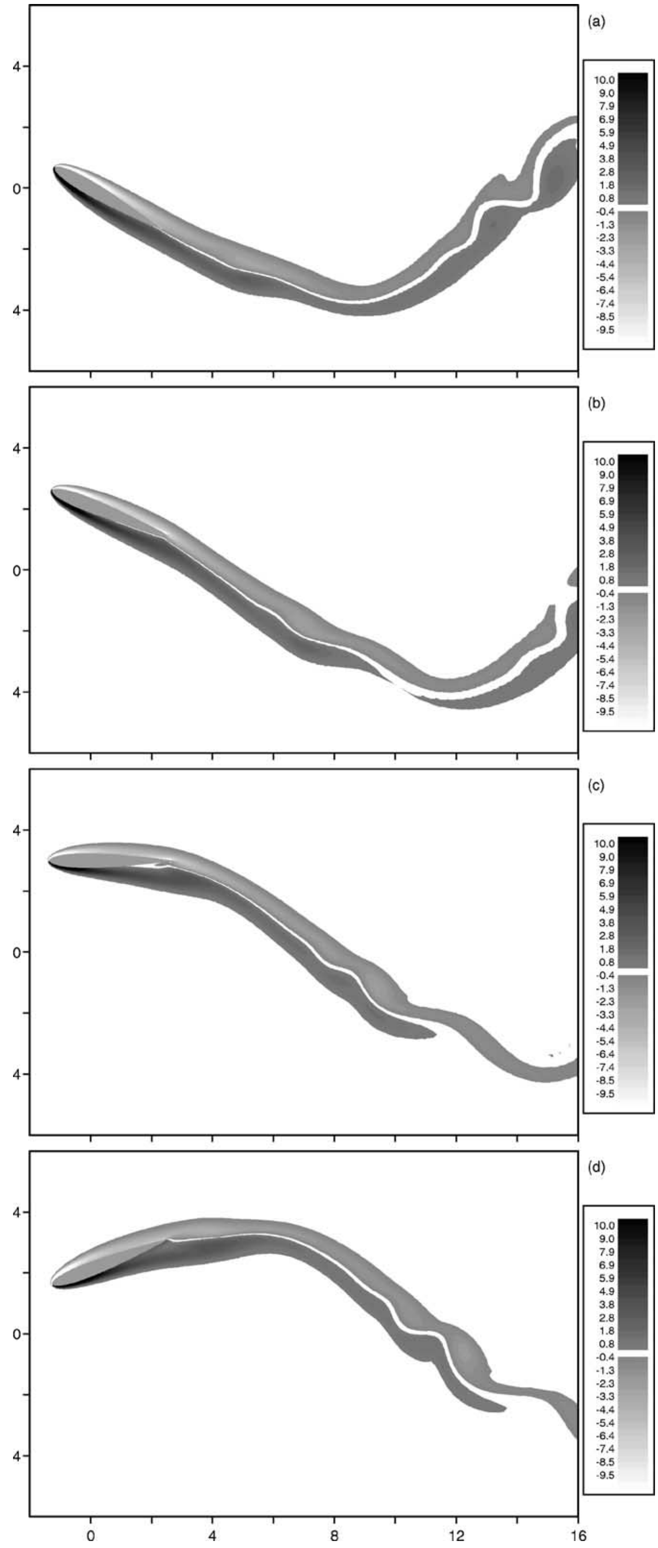

Fig. 13. Vorticity fields for $RE = 1100$, $\bar{\alpha} = 0°$, $\hat{A} = 3$, $\hat{\alpha} = -30°$, $\varphi = 90°$, $St = 0.225$, $\eta_P = 0.064$, $c_T = 0.02$, at (a) $t = 12.566$, (b) $t = 13.352$, (c) $t = 14.137$, (d) $t = 14.923$.

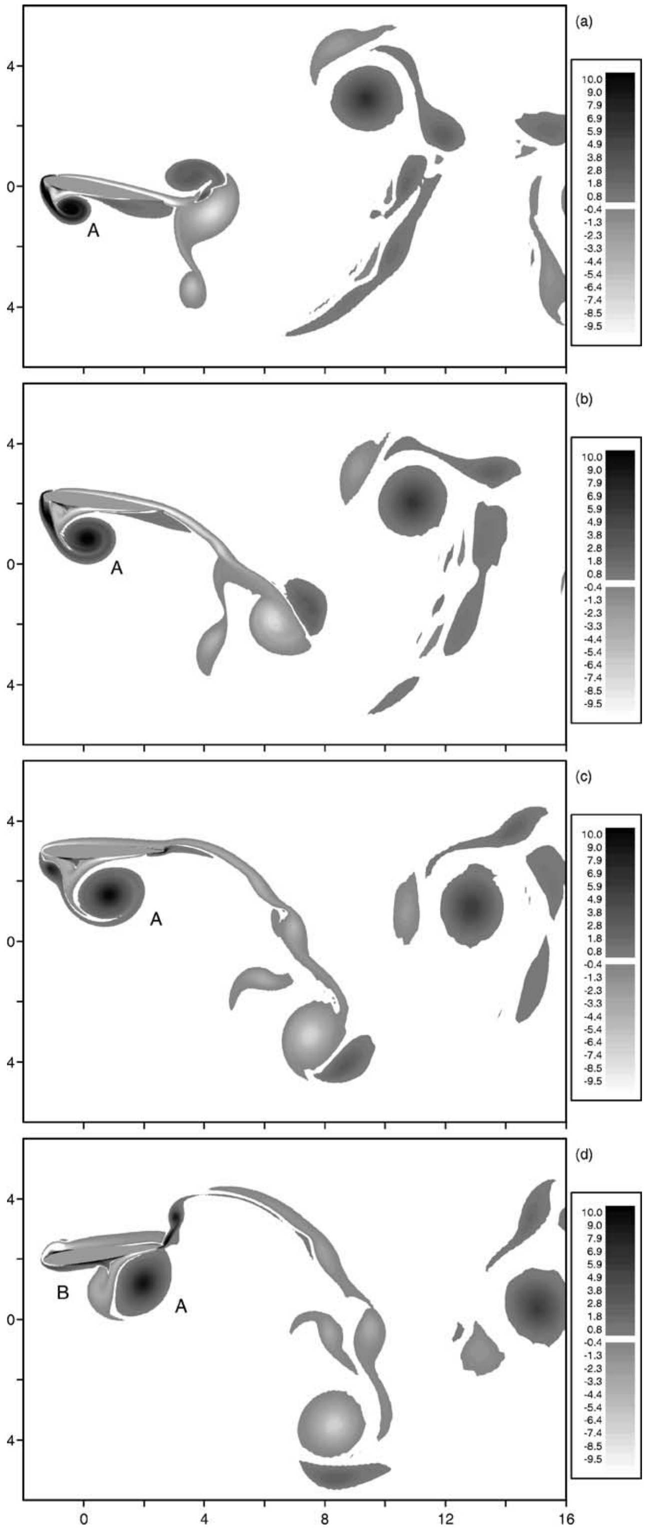

Fig. 14. Vorticity fields for $RE = 1100$, $\bar{\alpha} = 0°$, $\hat{A} = 3$, $\hat{\alpha} = -10°$, $\varphi = 90°$, $St = 0.5$, $\eta_P = 0.159$, $c_T = 1.04$, at (a) $t = 12.566$, (b) $t = 13.352$, (c) $t = 14.137$, (d) $t = 14.923$.

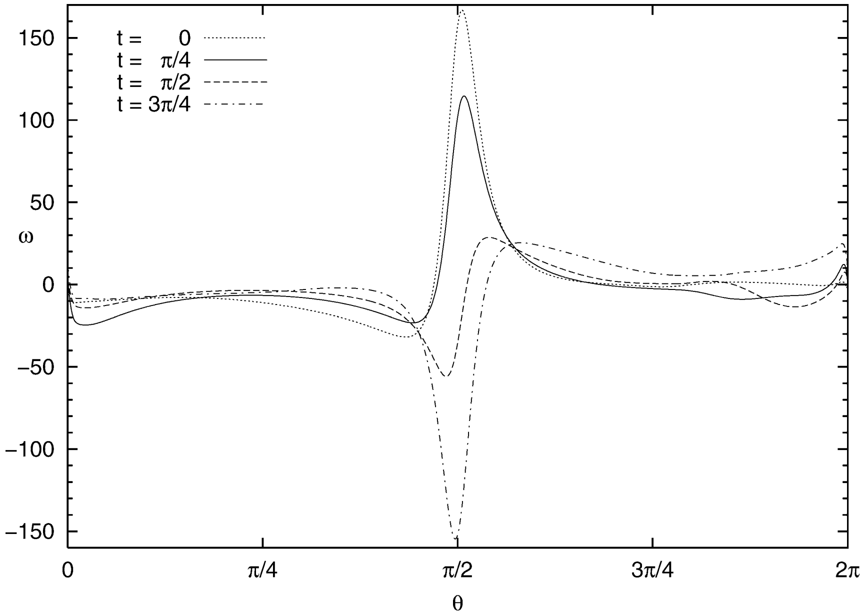

Fig. 15. Vorticity distribution along the foil profile, for $RE = 1100$, $\bar{\alpha} = 0°$, $\hat{A} = 3$, $\varphi = 90°$, $St = 0.35$, $\hat{\alpha} = -35°$.

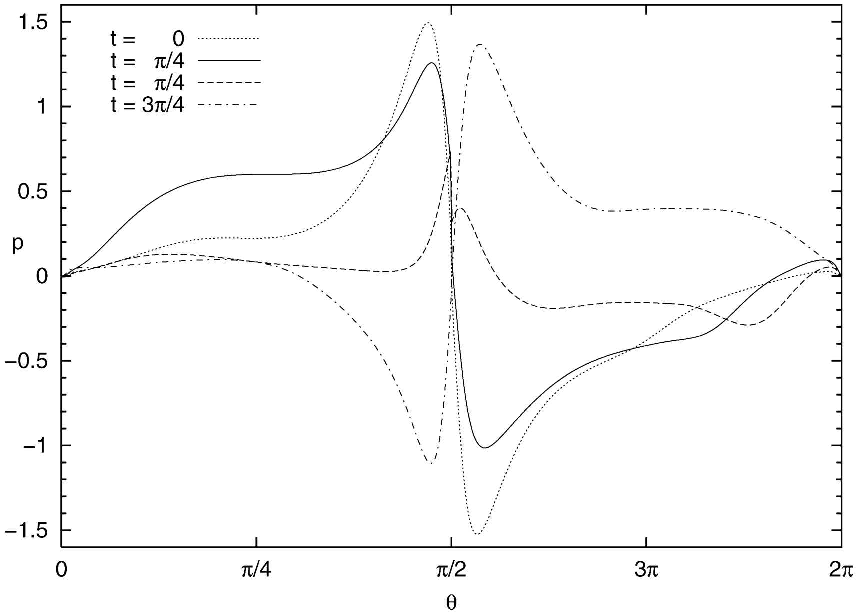

Fig. 16. Pressure distribution along the foil profile, for $RE = 1100$, $\bar{\alpha} = 0°$, $\hat{A} = 3$, $\varphi = 90°$, $St = 0.35$, $\hat{\alpha} = -35°$.

similar to those characterizing the measurements of Anderson et al. [26]. As discussed by Triantafyllou et al. [29], an analysis of fish swimming [30,31,1] shows that carangiform swimmers move their tail in such a way that its Strouhal number is close to 0.3–0.4. Moreover, the curves of η_P versus St are characterized by a slow decrease of η_P when the Strouhal number is increased beyond the value $St_{\max}$, while η_P quickly drops if St becomes smaller than $St_{\max}$. Since the thrust coefficient c_T monotonically increases with St (see Fig. 9), the present results suggest that it is usually better to work at values of St slightly larger than $St_{\max}$ even though a small decrease in the efficiency is present. Sometimes, results concerning c_T and η_P are presented by varying the value of the maximum angle of attack $\gamma_{\max}$. To allow an easy evaluation of the results shown in Figs. 9, 10 in terms of the maximum angle of attack, in Fig. 11 the propulsive efficiency η_P is plotted versus St for the same parameters of Fig. 10 but

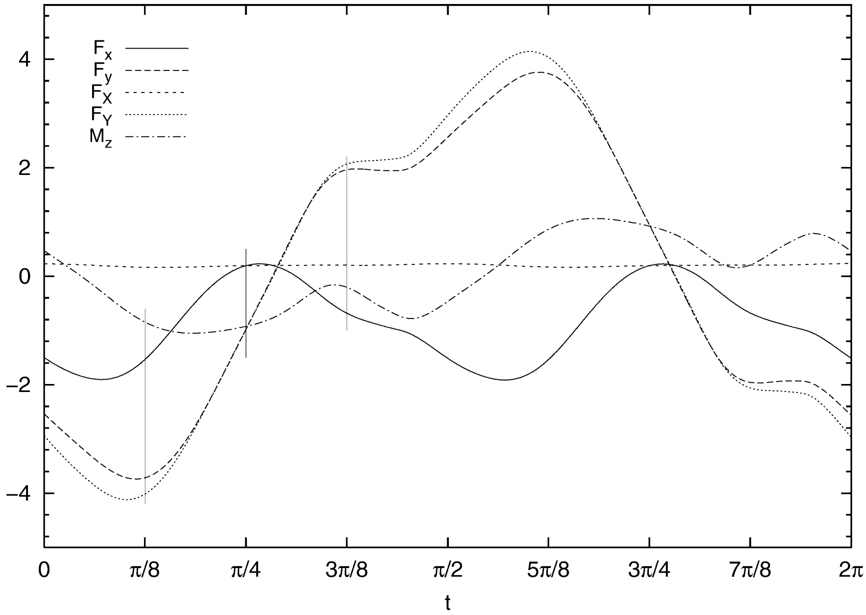

Fig. 17. Forces development on the foil during one period, for $RE = 1100$, $\bar{\alpha} = 0°$, $\hat{A} = 3$, $\varphi = 90°$, $St = 0.35$, $\hat{\alpha} = -35°$.

for constant values of $\gamma_{\max}$, equal to 5°, 10°, 20° and 30° respectively. Differently from the experimental data by Anderson et al. [26], the maximum propulsive efficiency is achieved for $\gamma_{\max}$ falling between 10° and 20°.

One of the main advantages of numerically simulating the phenomenon with respect to an experimental investigation is the access to the velocity and vorticity fields both in space and in time. This allows us to investigate in more detail the flow close to the foil and to gain a clear picture of the vortex structures which give rise to the maximum propulsive efficiency. Figs. 12–14 show the vorticity dynamics generated by the oscillating foil at four phases during half the cycle for three different cases, all with $RE = 1100$, $\bar{\alpha} = 0°$, $\varphi = 90°$. It is worth pointing out that the vorticity fields during the following half cycle are the mirror images of those shown in Figs. 12–14. In the first case (Fig. 12) we have $\hat{\alpha} = -35°$ and $St = 0.35$, the second one (Fig. 13) is characterized by $\hat{\alpha} = -30°$ and $St = 0.225$, the third one (Fig. 14) by $\hat{\alpha} = -10°$ and $St = 0.5$. The first case provides the maximum value of the propulsive efficiency, as it can be seen from Fig. 10, while the second and third ones give rise to low values of η_P. The analysis of flow visualizations clearly shows that the maximum efficiency is associated with a complex vorticity dynamics. At the beginning of the cycle a small positive (counterclockwise) vortex (vortex A) is present in the wake of the foil, but close to it (see Fig. 12(a)), being generated by the roll up of the vorticity shed by the trailing edge which moved downward. Then, this weak vortex is dissipated by viscous effects (see Fig. 12(b)–(d)). At $t = 13.352$, a weak flow separation close to the leading edge of the foil can be observed, which is associated with the generation of a weak back flow along the lower surface of the foil. The flow separation becomes more evident later on (see Fig. 12(c)). Then the free shear layer rolls up and gives rise to a new positive vortex structure (vortex B) which is then convected downstream. The time development of the vortex can be followed looking at Fig. 12(a) and considering the mirror image of vortex C with respect to a horizontal axis. The positive vortex, which is generated by flow separation at the leading edge, interacts with the negative (clockwise) vorticity shed by the trailing edge which moves upward. This interaction cuts the free shear layer feeding the main vortex which then leaves the foil. Then the counterclockwise vorticity shed by the foil gives rise to two new vortices of smaller strength (mirror image of vortices D and E). Hence three large vortex structures appear in the wake of the foil each half cycle.

Fig. 15, where the vorticity along the foil surface is plotted at the same phases as Fig. 12, shows that in the upper face of the foil negative vorticity is always present except close to the leading edge where, at the beginning of the cycle, large positive values can be detected. Simultaneously, along the lower face, weak negative vorticity appears in two small regions, suggesting the presence of flow separation. The first one is close to the leading edge while the second one is close to the trailing edge. At $t = 13.352$ the two regions merge and give rise to a significant back flow. Later on, the recirculating flow moves downstream and a coherent vortex structure is generated (see Fig. 12(c)). This strong vortex induces a secondary flow separation from the smooth surface of the foil and at $t = 14.923$ only positive vorticity is present in the lower face of the foil. The pressure distribution along the foil and the forces acting on the foil are shown in Figs. 16, 17. The force component in the x-direction is negative during a large part of the cycle, pushing the foil in the forward direction. The component in the y-direction opposes the transverse oscillations of the foil except when the foil leaves its maximum positions. Similarly the torque opposes the pitching

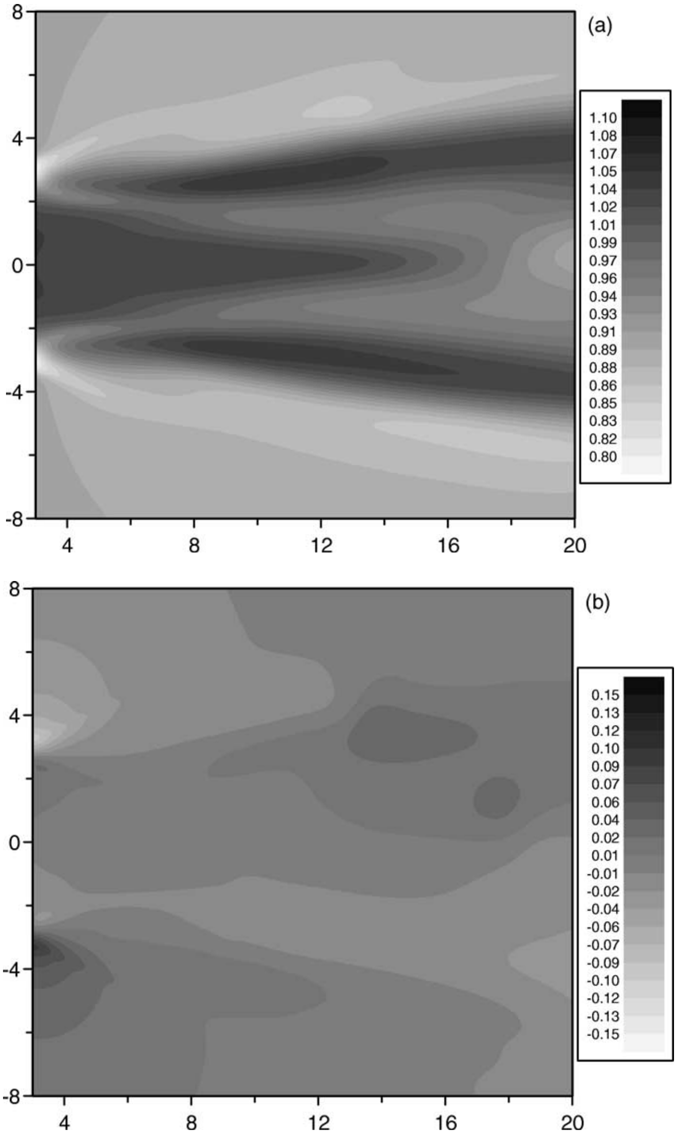

Fig. 18. Averaged velocity field, for $RE = 1100$, $\bar{\alpha} = 0^\circ$, $\hat{A} = 3$, $\varphi = 90^\circ$, $St = 0.35$, $\hat{\alpha} = -35^\circ$, (a) horizontal component u, (b) vertical component v.

oscillations, thus indicating that the propulsive thrust is obtained by a significant work performed on the foil. However, in the case under examination, the efficiency is good as shown by the results of Fig. 10.

A poor efficiency characterizes the cases plotted in Figs. 13, 14. For the lowest value of the Strouhal number the effects related to the forward velocity prevail on those induced by the transverse oscillations of the foil. Therefore the vorticity field resembles that behind a foil in steady forward motion, even though the wake is characterized by a waviness induced by the foil oscillations (see Fig. 13). In particular no significant vortex structures can be detected, except for vorticity patches generated by the instability of the wake, triggered by foil movements. On the other hand, a large number of vortex structures can be observed for the largest value of the Strouhal number (see Fig. 14). The vortices are generated both at the leading and trailing edges of the foil which move with large velocities when compared with U_0^*. From Fig. 14, it appears that in the wake of the foil a sequence of vortex pairs is present, which are generated during the previous cycles. To understand the process of generation, it necessary to follow the vorticity shed by the leading edge. The upward motion of the leading edge, which takes place at the beginning of the cycle, gives rise to a strong positive vortex (vortex A) which then grows and moves along the foil inducing a strong secondary separation. The free shear layer so generated rolls up and induces a new vortex of opposite circulation (vortex B) which couples

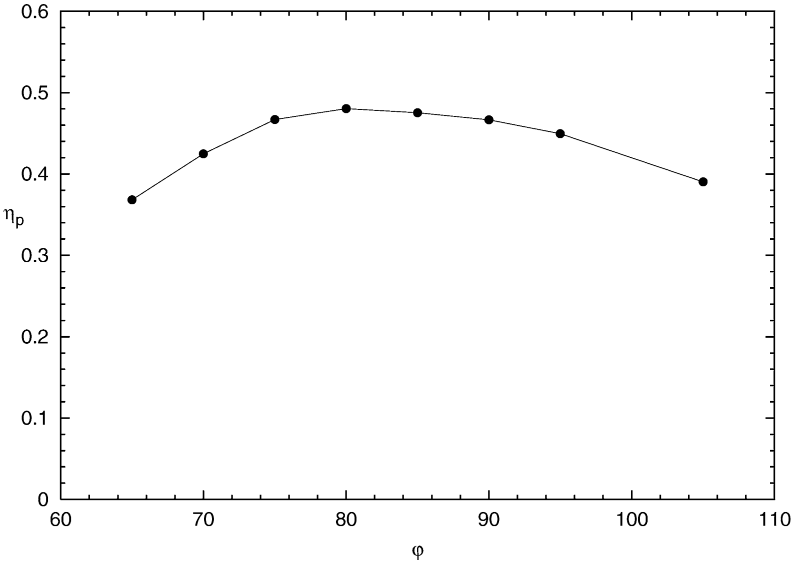

Fig. 19. Efficiency η_P plotted versus the phase angle φ, for $RE = 1100$, $\bar{\alpha} = 0°$, $\hat{A} = 3$, $St = 0.35$, $\hat{\alpha} = -35°$.

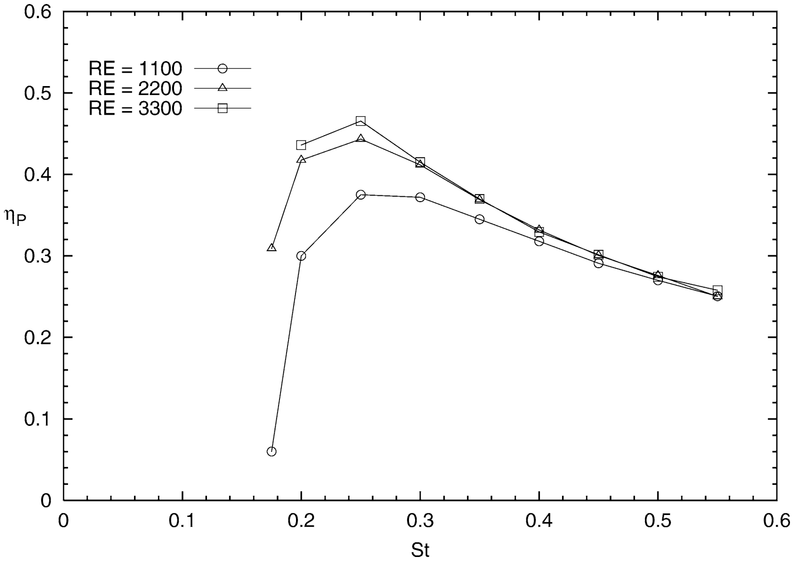

Fig. 20. Efficiency η_P plotted versus the Strouhal number, for $\bar{\alpha} = 0°$, $\hat{A} = 3$, $\varphi = 90°$, $St = 0.35$, $\hat{\alpha} = -20°$ and different values of the Reynolds number RE.

with the previous one and gives rise to a vortex pair which then moves because of the self-induced velocity and the free stream velocity. The main vortex is stronger than the secondary one, so that the latter tends to rotate around the former while moving downstream. Because of the strong nonlinear interaction of the different vortices, the flow field is quite complex. At this stage it is worth pointing out that both when the efficiency is high (Fig. 12) and for small values of η_P (Fig. 14) the vortex structures shed by the leading edge of the foil are as strong as those originated by the vorticity shed by the trailing edge. Therefore the obtained results suggest that an accurate description of the phenomenon can be gained only by means of an approach able to describe flow separation at the two edges of the foil.

As pointed out in the introduction, the thrust acting on the oscillating foil is physically produced by a jet of fluid which leaves the foil and moves in the opposite direction. This jet clearly appears when the flow is averaged in time (see Fig. 18, where the time averaged value of the velocity field induced by the oscillating foil is shown for the same values of the paramenters of Fig. 12). Taking into account that the dimensionless free stream velocity $U_0 = 1/(\pi St)$ is about 0.91, large downstream

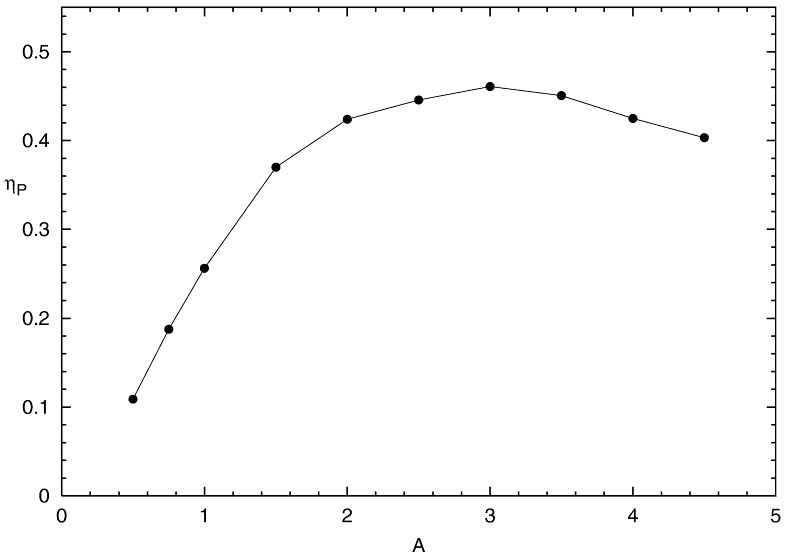

Fig. 21. Efficiency η_P plotted versus the dimensionless heave amplitude $\hat{A}$, for $RE = 1100$, $\bar{\alpha} = 0°$, $\varphi = 80°$, $St = 0.30$, $\hat{\alpha} = -30°$.

velocities can be detected behind the average location of the foil and at y equal to about ±3 which correspond to the maximum and minimum heave positions, where the main vortex structures leave the foil. From Fig. 18(b), it also appears that the mass flux that leaves the foil as a jet is compensated by slow moving fluid which approaches the foil on the two sides with vertical velocities.

A further set of runs has been made to investigate the propulsive efficiency when the phase angle φ between the heave and pitch oscillations is varied. We remind to the reader that the results shown in Figs. 9, 10 have been obtained for φ equal to 90°. As found experimentally by Anderson et al. [26], Fig. 19 shows that the maximum efficiency is obtained for values of φ around 80°. However, the values of η_P which are found in the numerical simulations are smaller than those measured by Anderson et al. [26].

The phenomenon has been also investigated varying $\hat{A}$ and the best propulsive efficiency has been obtained for values of $\hat{A}$ similar to those used by Anderson et al. [26] even though the efficiency is smaller. Indeed, Fig. 21, where η_P is plotted versus $\hat{A}$ for fixed values of the other parameters, shows that the maximum efficiency is obtained when $\hat{A}$ is approximatively equal to 3, i.e., approximately three quarters of the chord length, and the maximum value of η_P is equal to about 0.45. The relatively small values of η_P can be ascribed to the small Reynolds number used in the numerical simulations and hence to the large viscous effects which characterize the numerical results. Indeed, Fig. 20, where the propulsive efficiency is computed for different values of the Reynolds number, while keeping all the other parameters fixed, shows that increasing RE the maximum of η_P increases. These results suggest that at large Reynolds numbers, values of η_P closer to the experimental ones can be obtained. However, computatinal costs have not allowed the simulations for values of RE as large as the those characterizing Anderson et al.'s [26] experiments. Fig. 22 shows the vorticity field for values of the parameters providing a good efficiency, i.e., $RE = 1100$, $\bar{\alpha} = 0°$, $\hat{A} = 1$, $\hat{\alpha} = -30°$, $\varphi = 80°$, $St = 0.3$. The results show that high efficiency is associated with the generation of a moderately strong leading edge vortex which subsiquently amalgamate with the trailing edge vorticity generating a large vortex structure every half cycle. The amalgamation of the vorticity shed by the leading edge with that shed by the trailing edge takes place because the amplitude of the pitching and heaving oscillations and their phase shift are such that the advection of the counter-clockwise leading edge vorticity (vorticity patch A in Fig. 22(a)) along the lower foil surface (see Figs. 22(b)–(d)) brings it close to the trailing edge when the edge is going to start its downward motion and hence to generate further counter-clockwise vorticity (the reader can follow the subsequent development of the counter-clockwise vortex by considering the mirror images of Figs. 22(a)–(d), i.e., the time development of the mirror image of vortex B). The strong vortex structures generated by the foil every half cycle give rise to a reverse Karman street which resembles the wake behind bluff bodies but with vortices rotating in an opposite direction. Therefore the fluid behind the body is not retarded but strongly accelerated, as it appears from Fig. 23.

The results by Visbal and Shang [32] show that the flow field generated by a rapidly pitching foil is significantly dependent on the position of the pitching axis. Similarly the visualizations by Ohmi et al. [33], who analysed the flow generated by a foil set in motion impulsively and subject simultaneously to a constant translation and harmonic oscillations in pitch, show that the effects of the position of the pitching axis are especially marked. This because the displacement of the pitching axis is accompanied by variations of the rotation radius at the leading and trailing edges. Therefore it is likely that also the performances of pitching and heaving foils in steady forward motion are significantly affected by the position of the pitching axis. A final set of runs has

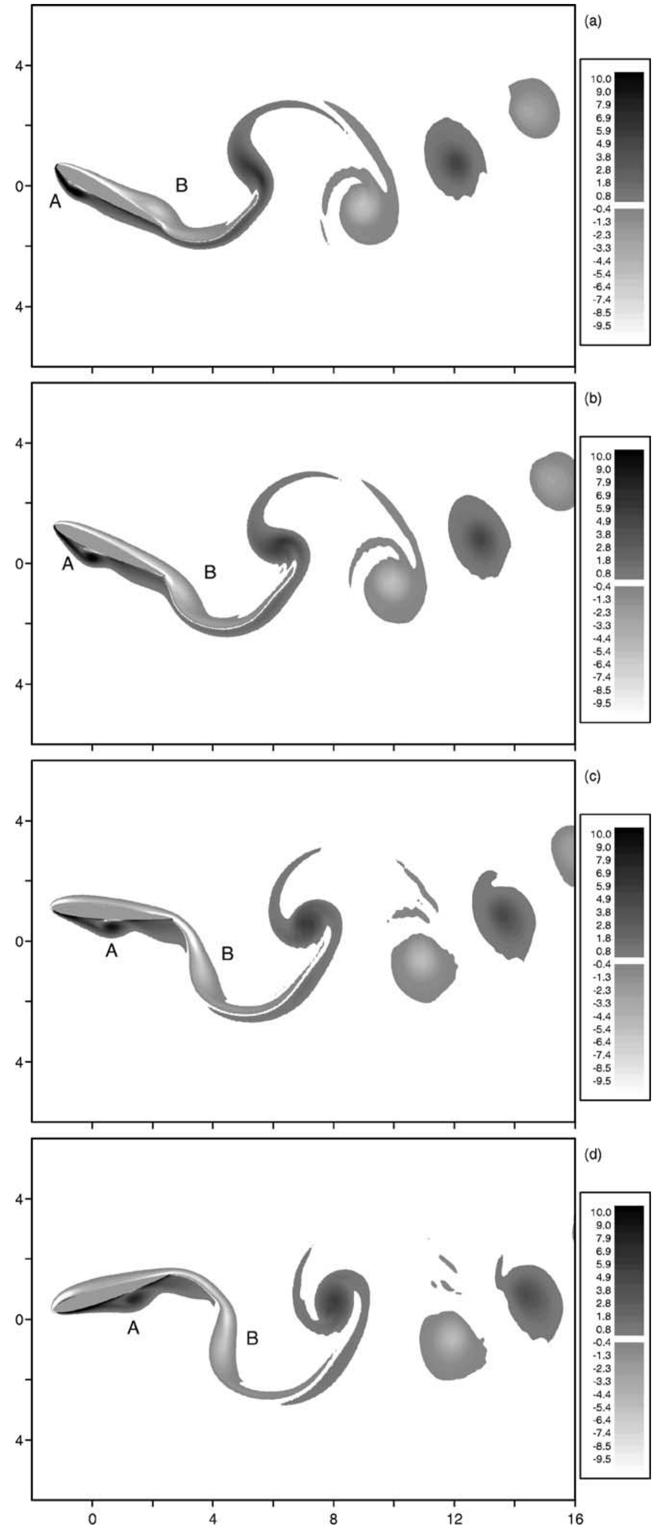

Fig. 22. Vorticity fields for $RE = 1100$, $\bar{\alpha} = 0°$, $\hat{A} = 1$, $\hat{\alpha} = -30°$, $\varphi = 80°$, $St = 0.3$, $\eta_P = 0.2562$, $c_T = 0.274$, at (a) $t = 12.566$, (b) $t = 13.352$, (c) $t = 14.137$, (d) $t = 14.923$.

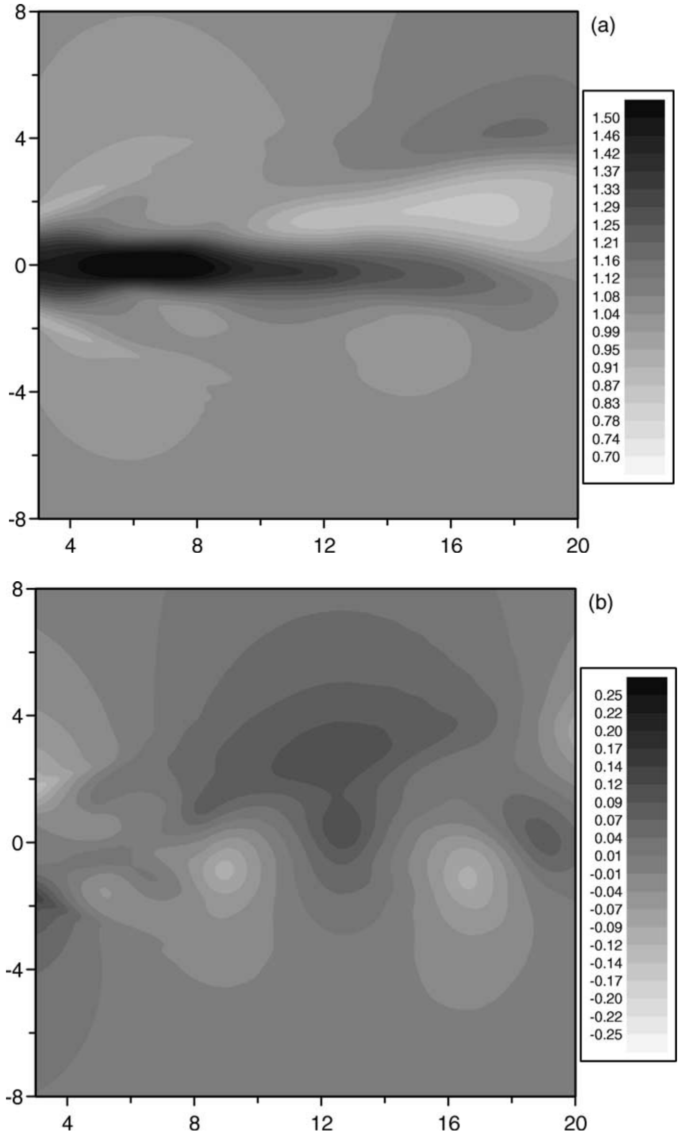

Fig. 23. Averaged velocity field, for $RE = 1100$, $\bar{\alpha} = 0°$, $\hat{A} = 1$, $\varphi = 80°$, $St = 0.3$, $\hat{\alpha} = -30°$, (a) horizontal component u, (b) vertical component v.

been made varying the value of d and the obtained values of the propulsive efficiency η_P are shown in Fig. 24. A maximum of η_P is present for d equal to about 0.666 and this finding provides support to the choice of Anderson et al. [26], who fixed the pitching axis at a distance from the leading edge equal to one third of the chord length.

4. Concluding remarks

The unsteady flow around a two-dimensional airfoil in steady forward motion and oscillating with a combination of harmonic heaving and pitching movements has been determinated by solving momentum equations in the ψ–ω formulation using a pseudo-spectral approach and finite-difference approximations. The investigation by Wang [16] has been extended by adding pitching oscillations to the foil motion. As pointed out by Wang [16] herself, the inclusion of the pitching motion is fundamental to understand the generation of large values of the thrust. Moreover, pitching oscillations are the only means to produce thrust by foils which operate in hovering mode or start to move. The versatile tool which has been developed has allowed

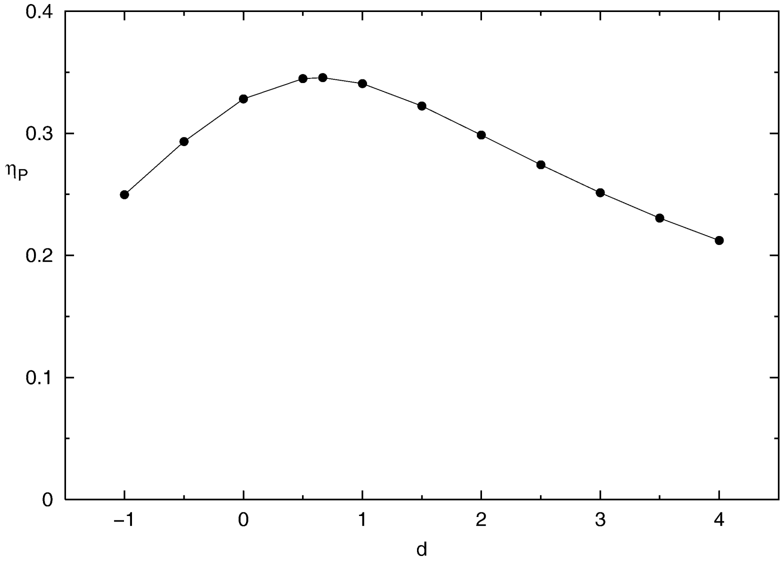

Fig. 24. Efficiency η_P plotted versus d, for $RE = 1100$, $\bar{\alpha} = 0°$, $\hat{A} = 1$, $\varphi = 80°$, $St = 0.30$, $\hat{\alpha} = -15°$.

the achievements of results for a large set of values of the paramenters and the identification of those giving rise to optimal propulsive performances even though only moderate values of the Reynolds number have been considered. The numerical results show conditions for optimal production of thrust, similar to those selected by Anderson et al. [26] on the basis of experimental measurements, even though slight differences are present which can be ascribed to the different values of the Reynolds number characterizing the numerical results and the experimental data.

Visualizations of the flow show that high efficiency accompanied by significant thrust is associated with the generation of moderately strong leading edge vortices, which subsiquently amalgamate with the trailing edge vorticity leading to the formation of vortex structures which give rise to a reverse Karman street. The phase angle between the heave and pitch motions and their amplitudes are of critical importance, because they determine the timing of the formation and shedding of the leading edge vortex with respect to the shedding of vorticity of the same sign by the trailing edge. Moreover, high efficiency and thrust coefficients are found to be associated with the generation of a concentrated jet of fluid leaving the foil in the opposite direction of its forward motion.

These findings are based on results obtained varying one parameter while keeping fixed the others. Hence for definitive conclusions a more exhaustive investigation of the phenomenon in the parameter space should be performed.

The present numerical approach can be easily extended to investigate aperiodic motions of the caudal fin of fishes performing fast starting and rapid maneuvering, in order to understand the optimal performances of fishes which are able to coordinate the transient motion of their body and tail minimazing the energy lost in the wake during starts and maneuvering [29]. Also the manipulation of ambient vorticity by moving foils can be investigated to understand how swimming fishes use their caudal fin to extract energy from the vorticity generated by their body thus recovering some of the work previously done. The control of vortices has been shown to be possible by the experiments made by Gopalkrishnan et al. [34].

Acknowledgements

The authors wish to thank Prof. M. Triantafyllou for discussions on various issues of the work. Thanks are also due to the Office of Naval Research for funding the research under contract N. 000140310193 monitored by Dr. Thomas F. Swean. Further financial support has been provided by the University of Genova. This work is part of the Ph.D. thesis of Laura Guglielmini to be submitted in partial fulfillment of her degree.

References

[1] M.J. Lighthill, Hydromechanics of aquatic animal propulsion, Annu. Rev. Fluid Mech. 1 (1969) 413–445.
[2] H. Ohashi, N. Ishikawa, Visualization study of flow near the trailing edge of an oscillating airfoil, Bull. JSME 15 (85) (1972) 840–847.

[3] Y. Oshima, K. Oshima, Vortical flow behind an oscillating foil, in: Proc. 15th IUTAM Int. Congress, North-Holland, 1980, pp. 357–368.

[4] Y. Oshima, A. Natsume, Flow field around an oscillating foil, in: W. Merzkirch (Ed.), Flow visualization II, Proc. Second Int. Symp. on Flow Visualization, Bochum, Germany, Hemisphere, 1980, pp. 295–299.

[5] M. Koochesfahani, Vortical patterns in the wake of an oscillating foil, AIAA J. 27 (1989) 1200–1205.

[6] T. Maxworthy, The fluid dynamics of insect flight, Annu. Rev. Fluid Mech. 13 (1981) 329.

[7] C.P. Ellington, The aerodynamics of hovering insect flight. IV Aerodynamic Mechanism, Philos. Trans. Roy. Soc. London Ser. B 305 (1984) 79–113.

[8] G.R. Spedding, The aerodynamics of flight, in: R.M. Alexander (Ed.), Mechanics of Animal Locomotion, Springer, 1992, p. 51.

[9] D.H. Choi, L. Landweber, Inviscid analysis of two-dimensional airfoils in unsteady motion using conformal mapping, AIAA J. 28 (12) (1990) 2025–2033.

[10] K. Streitlien, G.S. Triantafyllou, M.S. Triantafyllou, Efficient foil propulsion through vortex control, AIAA J. 34 (1996) 2315–2319.

[11] P. Liu, N. Bose, Propulsive performance from oscillating propulsors with spanwise flexibility, Proc. Roy. Soc. London 453 (1997) 1763–1770.

[12] M. Wolfgang, J.M. Anderson, M.A. Grosenbaugh, D.K.P. Yue, M.S. Triantafyllou, Near-body flow dynamics in swimming fish, J. Exp. Biol. 202 (1999) 2303–2327.

[13] T.J. Pedley, S.J. Hill, Large-amplitude undulatory fish swimming: fluid mechanics coupled to internal mechanics, J. Exp. Biol. 202 (1999) 3431–3438.

[14] Q. Zhu, M.J. Wofgang, D.K. Yue, M.S. Tiantafyllou, Three-dimensional flow structures and vorticity control in fish-like swimming, J. Fluid Mech. 468 (2002) 1–28.

[15] J.A. Ekaterinaris, M.F. Platzer, Computational predictor of airfoil dynamic stall, Prog. Aerospace Sci. 33 (1997) 759–846.

[16] Z.J. Wang, Vortex shedding and frequency selection in flapping flight, J. Fluid Mech. 410 (2000) 323–341.

[17] M. Braza, P. Chassaing, H. Ha Minh, Numerical study and physical analysis of the pressure and velocity fields in the near wake of a circular cylinder, J. Fluid Mech. 165 (1986) 79–130.

[18] A. Borthwick, Comparison between two finite-difference schemes for computing the flow around a cylinder, Int. J. Numer. Methods Fluids 6 (1986) 275–290.

[19] C. Hirsch, Numerical Computation of Internal and External Flows, Wiley, 1988.

[20] B.P. Leonard, A survey of finite differences of opinion on numerical modelling of the incomprehensible defective confusion equation, in: Proc. ASME Winter Annual Meeting, Publ. AMD-34, 1979.

[21] A. Thom, An investigation of fluid flow in two dimensions. Aerospace Research Center R. and M., No.1194, United Kingdom, 1928.

[22] P.J. Roache, Computational Fluid Dynamics, Hermosa, 1972.

[23] G.B. Deng, E. Guilmineau, J. Piquet, P. Quentey, M. Visonneau, Computation of unsteady laminar viscous flow past an airfoil using the CPI method, Int. J. Numer. Methods Fluids 19 (1994) 765–794.

[24] W.Z. Shen, T.P. Loc, Simulation of 2d external viscous flows by means of a domain decomposition method using an influence matrix technique, Int. J. Numer. Methods Fluids 20 (1995) 1111–1136.

[25] J.L. Guermond, L. Quartapelle, Uncoupled ω–Ψ formulation for plane flows in multiply connected domains, Math. Models Methods Appl. Sci. 7 (6) (1997) 731–767.

[26] J.M. Anderson, K. Streitlien, D.S. Barrett, M.S. Triantafyllou, Oscillating foils of high propulsive efficiency, J. Fluid Mech. 360 (1998) 41–72.

[27] P. Blondeaux, G. Vittori, A route to chaos in an oscillatory flow: Feigenbaum scenario, Phys. Fluids A 3 (1991) 2492.

[28] G. Vittori, P. Blondeaux, Quasiperiodicity and phase locking route to chaos in the 2-D oscillatory flow around a circular cylinder, Phys. Fluids A 5 (8) (1993) 1866.

[29] M.S. Triantafyllou, G.S. Triantafyllou, D.K.P. Yue, Hydrodynamics of fishlike swimming, Annu Rev. Fluid Mech. 32 (2000) 33–53.

[30] M.S. Triantafyllou, G.S. Triantafyllou, M.A. Grosenbaugh, Optimal thrust development in oscillating foils with application to fish propulsion, J. Fluids Structures 7 (1993) 205–224.

[31] J.J. Rohr, E.W. Hendricks, L. Quigley, F.E. Fish, J.W. Gilpatrick, J. Scardina-Ludwing, Observations of dolphin swimming speed and Strouhal number, Space Nav. Warfare Syst. Ctr. Tech. Rep. 1769, San Diego, 1998.

[32] M.R. Visbal, J.S. Shang, Investigation of the flow structure around a rapidly pitching airfoil, AIAA J. 27 (1989) 1044–1051.

[33] K. Ohmi, M. Coutanceau, O. Daube, T.P. Loc, Further experiments on vortex formation around an oscillating and translating airfoil at large incidences, J. Fluid Mech. 211 (1991) 37–60.

[34] R. Gopalkrishnan, M.S. Triantafyllou, G.S. Triantafyllou, D.S. Barrett, Active vorticity control in a shear flow using a flapping foil, J. Fluid Mech. 274 (1994) 1–21.